Exploring the Dust Content of Galactic Halos with *Herschel*. IV. NGC 3079

S. Veilleux,[1,2] ⋆ M. Meléndez,[1,3] M. Stone,[1] G. Cecil,[4] E. Hodges-Kluck,[5] J. Bland-Hawthorn,[6] J. Bregman,[7] F. Heitsch,[4] C. L. Martin,[8] T. Mueller,[9] D. S. N. Rupke,[10] E. Sturm,[9] R. Tanner,[4,11] C. Engelbracht[12]

[1]*Department of Astronomy, University of Maryland, College Park, MD 20742, USA*
[2]*Joint Space-Science Institute, University of Maryland, College Park, MD 20742, USA*
[3]*Space Telescope Science Institute, Baltimore, MD 21218, USA*
[4]*Department of Physics and Astronomy, University of North Carolina, Chapel Hill, NC 27599, USA*
[5]*X-ray Astrophysics Laboratory, NASA Goddard Space Flight Center, Greenbelt, MD 20771, USA*
[6]*Department of Physics, University of Sydney, Sydney, NSW 2006, Australia*
[7]*Department of Astronomy, University of Michigan, Ann Arbor, MI 48109, USA*
[8]*Department of Physics, University of California, Santa Barbara, CA 93106, USA*
[9]*Max-Planck-Institute for Extraterrestrial Physics (MPE), 85748 Garching, Germany*
[10]*Department of Physics, Rhodes College, Memphis, TN 38112, USA*
[11]*Universities Space Research Association, 7178 Columbia Gateway Dr., Columbia, MD 21046, USA*
[12]*Department of Astronomy, University of Arizona, Tucson, AZ 85721, USA*

ABSTRACT

We present the results from an analysis of deep *Herschel* far-infrared observations of the edge-on disk galaxy NGC 3079. The PSF-cleaned PACS images at 100 and 160 μm display a 25×25 kpc^2 X-shape structure centered on the nucleus that is similar in extent and orientation to that seen in Hα, X-rays, and the far-ultraviolet. One of the dusty filaments making up this structure is detected in the SPIRE 250 μm map out to ∼ 25 kpc from the nucleus. The match between the far-infrared filaments and those detected at other wavelengths suggests that the dusty material has been lifted out of the disk by the same large-scale galactic wind that has produced the other structures in this object. A closer look at the central 10×10 kpc^2 region provides additional support for this scenario. The dust temperatures traced by the 100-to-160 μm flux ratios in this region are enhanced within a biconical region centered on the active galactic nucleus, aligned along the minor axis of the galaxy, and coincident with the well-known double-lobed cm-wave radio structure and Hα-X-ray nuclear superbubbles. PACS imaging spectroscopy of the inner 6-kpc region reveals broad [C II] 158 μm emission line profiles and OH 79 μm absorption features along the minor axis of the galaxy with widths well in excess of those expected from beam smearing of the disk rotational motion. This provides compelling evidence that the cool material traced by the [C II] and OH features directly interacts with the nuclear ionized and relativistic outflows traced by the Hα, X-ray, and radio emission.

Key words: galaxies: halos – galaxies: ISM – galaxies: photometry – galaxies: starburst – galaxies: star formation – galaxies: infrared: galaxies

1 INTRODUCTION

There is growing evidence that galaxies are dynamically and chemically evolving systems where gas flows in and out, or is processed into stars (Tumlinson et al. 2017; Péroux & Howk 2020; Veilleux et al. 2020). Galaxies acquire gas from galaxy mergers, galactic

fountains, and intergalactic accretion, but may also lose material in large-scale outflows driven by stellar and black-hole driven processes. The dust, tied to the outflowing gas by strong electrostatic forces, likely also participates in this large-scale motion. The amount of dust outside of galaxies, inferred from reddening measurements of background quasars and galaxies by foreground galaxy halos, is comparable to that within galaxies (Ménard et al. 2010; Peek et al. 2015), but the origin of this dust is uncertain. Presumably made in-

⋆ E-mail: veilleux@astro.umd.edu

side galaxies, this dust was likely transported into the halos via tidal and ram-pressure stripping or large-scale outflows. Direct evidence for dusty outflows that extend on the scales of the circumgalactic medium (CGM; $\lesssim$ 100 kpc) and intergalactic medium (IGM; $\gtrsim$ 100 kpc) remains elusive, although this is changing (e.g., Rupke et al. 2019; Hodges-Kluck et al. 2020; Burchett et al. 2021).

The present paper is the fourth in a series that reports the results from a program conducted with the *Herschel* Space Observatory which examines the dust content of nearby galaxies with known galactic winds. Earlier papers have targeted the edge-on star-forming disk galaxies NGC 4631 (Meléndez et al. 2015, Paper I) and NGC 891 (Yoon et al. 2021, Paper III), and a number of star-forming dwarf galaxies highlighted by NGC 1569 (McCormick et al. 2018, Paper II). The target of the present paper is NGC 3079, a nearby ($z = 0.0037$) edge-on ($i = 82°$; Veilleux et al. 1999) disk galaxy with multi-wavelength evidence for a bisymmetric nuclear outflow. Warm ionized gas superbubbles (Ford et al. 1986; Filippenko & Sargent 1992; Veilleux et al. 1994; Cecil et al. 2001) with tightly correlated hot ionized gas (Cecil et al. 2002) have been observed along the minor axis (P.A. = 75°) of the galaxy disk, accompanied with a figure-8/double-lobe relativistic radio structure (Duric et al. 1983; Irwin & Seaquist 1988; Irwin et al. 2019; Sebastian et al. 2019) and extended nonthermal hard X-ray emission (Li et al. 2019).

There is some ambiguity about the driving mechanism (starburst or AGN) of this outflow. There is plenty of molecular gas in the central core of this galaxy to fuel star formation (Young et al. 1988; Sofue et al. 2001; Koda et al. 2002) and the implied central star formation rate (SFR) from *Akari* (2.6 $M_\odot$ yr^{-1}; Yamagishi et al. 2010) may be sufficient to drive the outflow, but this value is derived while ignoring the AGN contribution to the infrared emission. Excess $20 - 100$ keV continuum emission (Iyomoto et al. 2001) and strong 6.4 keV Fe K line emission (Cecil et al. 2002) point to the presence of an obscured AGN with a high hydrogen column density ($N_H \approx 10^{24.4-24.6}$ cm^{-2}; Brightman et al. 2015; Masini et al. 2016; Ricci et al. 2017), consistent with the picture of a nearly edge-on nuclear molecular disk responsible for the H_2O megamaser on parsec scale (Kondratko et al. 2005). A radio continuum emitting jet at centimeter wavelengths is seen working its way out of the innermost 1 to 2 pc clumpy region around the central AGN (Irwin & Seaquist 1988; Trotter et al. 1998; Yamauchi et al. 2004; Middelberg et al. 2007). Cecil et al. (2001) have shown that the very broad optical line emission at the base of the NE Hα bubble is positioned along the position angle of the inner radio jet, and thus have favored a scenario where the kinetic energy from the AGN jet is deposited (thermalized) at the base of the bubble and ultimately drives the observed biconical outflow (see also Middelberg et al. 2007). This same outflow, regardless of its exact origin, is almost certainly responsible for the broad but shallow blueshifted (by up to 600 km s^{-1}) H I 21-cm absorption in this system (Shafi et al. 2015).

The bisymmetric outflow of NGC 3079 has long been suspected to extend beyond 10 kpc based on the detections of faint large-scale extraplanar optical-line filaments (Heckman et al. 1990; Veilleux et al. 1995; Cecil et al. 2001), long-wavelength radio emission (Irwin & Saikia 2003), and soft X-ray structures (Fabbiano et al. 1992; Strickland et al. 2004a). The cometary H I 21-cm plume of the companion NGC 3073, located within the western biconical outflow ~ 50 kpc from NGC 3079 (Irwin et al. 1987; Shafi et al. 2015), has provided indirect evidence that the outflow may extend considerable further. This was recently confirmed by Hodges-Kluck et al. (2020), who examined deep archival *XMM-Newton* X-ray images and *GALEX* NUV and FUV maps and revealed the existence of a 60-kpc biconical structure of hot ionized and dusty material aligned along the central kpc-scale outflow.

The main objective of the present paper is to examine the cool ($T \simeq 10 - 1000$ K) dust and gas associated with both the small- and large-scale outflows in NGC 3079. We first present deep *Herschel* far-infrared images that trace the continuum emission from dust on large scale, and then search for cool gas impacted by the nuclear outflow using far-infrared imaging spectroscopy of [C II] 157.74 μm ([C II] 158 for short) and the OH 119.233, 119.441 μm doublet (OH 119 for short). Section 2 describes the observations and data processing. Section 3 presents the main results. Section 4 provides a more detailed and quantitative analysis of these results, and compares the *Herschel* data with some of the latest data at other wavelengths, on both small and large scales. The results of these comparisons are discussed against theoretical predictions of dust and cool gas entrainment and in the more general context of galaxy evolution and galaxy ecosystems. Section 5 summarizes the main conclusions. In this paper we adopt a distance of 19 Mpc for NGC 3079 (Springob et al. 2007), which corresponds to a scale of ~ 91 pc per arcsecond.

2 OBSERVATIONS AND DATA PROCESSING

2.1 Deep Far-Infrared Imaging

NGC 3079 was imaged with both the Photodetector Array Camera and Spectrometer (PACS; Poglitsch et al. 2010) and the Spectral and Photometric Imaging Receiver (SPIRE; Griffin et al. 2010) on board *Herschel* as part of our cycle 1 open-time program (OT1_sveilleu_2, PI: S. Veilleux; Table 1). For the PACS observations, we obtained simultaneous imaging in the PACS "green" 100 μm ($85 - 130$ μm) and "red" 160 μm ($130 - 210$ μm) channels in scan mode along six position angles at 55°, 70°, 85°, 95°, 110°, and 125° (Obs IDs: 1342231542, 1342231544, 1342231545, 1342231546, 1342231547, and 1342231543, respectively). At each orientation angle, we requested 60 scan legs of 4.′0 length, 4.″0 scan leg separation, a repetition factor of two, and a scan speed of 20″ s^{-1}. The total time per position angle, including telescope overhead, was ~ 1.6 hours, for a total request of 9.3 hours. The SPIRE observations (Obs ID: 1342221916 from the same program) were taken simultaneously at 250, 350, and 500 μm in large map mode covering an area of 30′ × 30′ with two repetitions at nominal speed (30″ s^{-1}).

The reduction of the PACS photometric data was done using the *Herschel* Interactive Processing Environment (HIPE; Ott 2010) version 8.0, following the exact same procedure as that used in Paper I. We only summarize the important steps here and refer the reader to Paper I for more details. We followed the standard pipeline procedure to convert from Level 0 to Level 1 data, including the extraction of the calibration tree needed for the data processing, correction for electronic crosstalk, application of the flat-field correction, and finally deglitching and conversion from Volts to Janskys per array pixel. To correct for bolometer drift (low frequency noise), both thermal and non-thermal (uncorrelated noise), and to create the final maps from the Level 1 data, we used the algorithm implemented in *Scanamorphos* (v21.0; Roussel 2013), which makes use of the redundancy built in the observations to derive the brightness drifts. The final PACS maps have a pixel size of ~ 1/4 of the PSF FWHM, i.e., 1.″7 at 100 μm and 2.″85 at 160 μm. *Scanamorphos* also produces error and weight maps. The error map is defined as the error on the mean brightness in each pixel. Note that it does not include any error propagation associated with the different steps performed

Table 1. Summary of the Observations

Instrument/mode	Waveband [μm]	t_{exp}[s]	Obs ID	Program ID
(1)	(2)	(3)	(4)	(5)
PACS/photometer	100	33576	1342231542-47	OT1_sveilleu_2
PACS/photometer	160	33576	1342231542-47	OT1_sveilleu_2
SPIRE/photometer	250	2929	1342221916	OT1_sveilleu_2
SPIRE/photometer	350	2929	1342221916	OT1_sveilleu_2
SPIRE/photometer	500	2929	1342221916	OT1_sveilleu_2
PACS/spectrometer	[C II] 158, OH 119	8045	1342221391	DDT_esturm_4

Column (1): Instrument / mode of observation; Column (2): Waveband or central wavelength of the spectral scan in the rest-frame of NGC 3079 in μm; Column (3): Exposure time in seconds; Column (4): Observation ID; Column (5): Program ID.

on the pipeline. Given the relatively small field of view of our observations, relative to the size of the galaxy, and the observing strategy, we created the *Scanamorphos* maps with the "minimap" and "flat" options. On the other hand, the SPIRE data was processed from level 0 up to level 1 with the HIPE scripts included in the *Scanamorphos* distribution. The preprocessing by the pipeline includes the same steps as in the PACS pipeline except that the conversion to brightness is in Janskys per beam and the thermal drifts are subtracted by using the smoothed series of thermistors located on the detector array as the input of the drift model (see Ott 2010, for details). To convert the SPIRE data from Jy per beam to Jy per pixel, we used the pipeline beam area as provided in the SPIRE Data Reduction Guide, Table 6.9 (SPIRE-RAL-DOC 003248, 23 Nov 2016), i.e., 469.3542, 831.275, 1804.3058 arcsec^2 at 250, 350, and 500 μm, respectively. The final SPIRE maps have a pixel size of $\sim$ 1/4 of the PSF FWHM, i.e., 4''.5, 6''.25, and 9''.0 at 250, 350, and 500 μm, respectively.

2.2 Far-Infrared Imaging Spectroscopy

The PACS spectroscopic observations of NGC 3079 were obtained as part of Director's Discretionary Time program DDT_esturm_4 (PI: E. Sturm, Obs ID 1342221391; Table 1). These observations were done in pointed observing mode with the PACS range scan spectroscopy Astronomical Observing Template (AOT). A medium chopper throw was used and the total on-source exposure time was 8045 seconds, resulting in a slightly irregular 5 × 5 grid of 9''.4 spaxels, where each spectrum covers redshifted [C II] 158 μm and the OH 119 μm doublet, among other features, with a spectral resolution $R \simeq 240$ and angular resolution of $\sim$ 11''.5 (estimated from Fig. 8 in the PACS Spectroscopy Performance and Calibration Guide Issue 3.0).

The PACS spectroscopic data were retrieved from the *Herschel* Science Archive (HSA)[1] via HIPE v15.0.0. These data have been pipeline-processed at the *Herschel* Science Centre with the Standard Product Generation (SPG) software v14.2.0 up to the *rebinnedCube* task. The standard reduction steps include glitch masking, bad and noisy pixel masking, dark and background subtraction, spectral flatfielding, and flux calibration to Jy per spaxel.

The [C II] data cubes were interpolated onto a regular spatial grid of 1'' spaxels. For each spaxel in the [C II] data, a second-order polynomial was fit to the continuum emission and subtracted from the spectrum. Two Gaussian components were then fit to the

continuum-subtracted spectrum and line profile properties are estimated using the sum of the two components. The uncertainty on the absolute flux calibration is of the order $\sim$ 6% and the wavelength calibration uncertainty for the red channel is $\sim$ 20 km s^{-1} (Poglitsch et al. 2010). Note however that for pointed observations the (original) spaxel size of 9''.4 is not small enough to spatially sample the beam well (the beam FWHM is $\sim$ 10''). The data are therefore undersampled and the true morphology of an object will be degraded. Nevertheless, a comparison of the published [C II] fluxes, velocities, and line widths measured from the PACS [C II] data of M 82 obtained in raster mode where the sky was Nyquist sampled (Contursi et al. 2013) against those derived by fitting two Gaussians to the interpolated data of the same object and same line obtained in the pointed mode provides confidence in the use of such interpolated data cubes from pointed observations (typically, the fluxes agree to within 10-25% while the velocity centroids and line widths agree to within 10% of the instrumental velocity resolution; Stone 2020).

The OH data cube of NGC 3079 was reduced in the same manner as the [C II] data cube, except that it was not interpolated to smaller spaxels to avoid erasing the abrupt changes in the absorption / emission line profiles observed in the data cube from spaxel to spaxel (discussed in Sec. 3.2.2). For each spaxel, a first-order spline was fit to the continuum emission and subtracted from the spectra. Profile fitting of the OH 119 doublet followed a similar procedure from Veilleux et al. (2013) and Stone et al. (2016). The OH doublet profile is modeled using four Gaussian components (two for each line of the doublet). The separation between the two lines of the doublet was set to 0.208 μm in the rest frame ($\sim$ 520 km s^{-1}) and the amplitude and standard deviation were fixed to be the same for each component in the doublet. The uncertainties on the measurements of the fluxes, centroid velocities, and velocity widths are estimated to be of the order $\sim$ 10%, 25 km s^{-1}, and 50 km s^{-1}, respectively, in the strongest features, but are considerably larger in the weaker features (see Sec. 3.2.2).

3 RESULTS

3.1 PACS and SPIRE Far-Infrared Maps

The PACS 100 μm and 160 μm images of NGC 3079 are shown in the left panels of Figure 1. Diffraction spikes associated with the central source are present in these data and need to be removed before we can make any quantitative statement about the extraplanar dust in this system. To remove the diffraction spikes, we follow the procedure detailed in McCormick et al. (2018). We employ a

[1] http://www.archives.esac.esa.int/hsa/whsa/
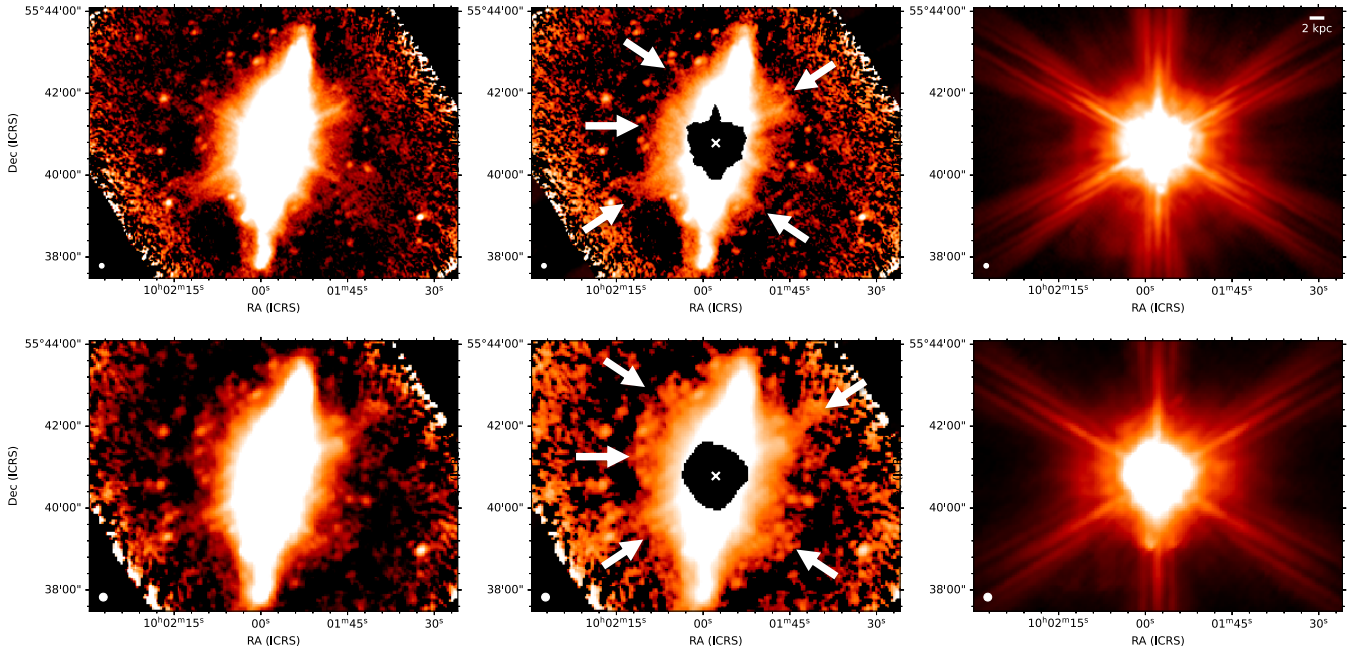
Figure 1. Deep PACS 100 μm (top row) and 160 μm (bottom row) images of NGC 3079. North is up and East to the left. The beam FWHM is displayed in the lower left corner of each panel. The linear scale is shown in the upper right panel. The left panels display the output from HIPE and *Scanamorphos*. The central panels show the results after removal of the diffraction spikes from the bright central source. The central region masked in black represents 95% of the total flux of the reference PSF. The right panels show the final PSF produced by combining the instrumental PSF at each peak pixel found by the CLEAN algorithm (not on the same intensity scale as the left and middle panels). In other words, (left panel) = (middle panel) + (right panel). All panels are on an arcsinh intensity scale. The white arrows point to extraplanar features detected in the CLEANED images.

modified version of the CLEAN algorithm[2] (Högbom 1974). Our CLEAN algorithm finds the peak pixel within an area similar to the disk region, subtracts the appropriate PSF scaled by a pre-defined gain as a fraction of the peak pixel value, and repeats these two steps until the peak pixel value meets or drops below a pre-defined minimum threshold value. Once the minimum threshold value is reached, the algorithm outputs the component and residual images. The reference PSFs for PACS[3] are chosen as our beam PSFs. The PSFs are rotated to match the galaxy observations, centered on their central pixels, and scaled by normalizing their central peak pixels to a value of unity for gain multiplication. Finally, we apply our CLEAN algorithm to each of the PACS and SPIRE images iteratively, lowering the threshold value to determine circumgalactic flux value convergence.

Figure 1 illustrates the "before" (left panels) and "after" (middle panels) results of applying our CLEAN algorithm to the PACS maps of NGC 3079. The diffraction spikes (shown in the right panels) are more prominent at 100 μm than at 160 μm, and become negligible in the SPIRE maps at 250 μm and beyond. This is a sign that the spectral energy distribution (SED) of the central energy source (AGN + nuclear starburst) in NGC 3079 is steeply declining at longer wavelengths. This is different from our results on the star-forming dwarf galaxies where no obvious trend was found with wavelength (McCormick et al. 2018).

The cleaned 100 and 160 μm maps (middle panels in Fig. 1) show a X-shape structure that is not associated with residuals from

the PSF. This structure extends over a scale of $\sim 25 \times 25$ kpc^2 centered on the nucleus but is not pointing back to the nucleus. Instead the filaments originate at the base of the stellar disk at a galactocentric radius of ~ 5 kpc on both sides from the nucleus. The filament in the SW quadrant is also detected in the SPIRE 250 μm image (Fig. 2), extending out ~ 25 kpc from the nucleus along PA = 215° or ~ 15 kpc from the mid-plane of the galaxy. The filament in the NW quadrant may also be detected in this image but it is within the confusion noise of the data.

Next, we estimate the far-infared fluxes emitted by these extraplanar features. The results are listed in Table 2. While the dust masses derived from these fluxes are discussed later in Section 4.1, here we discuss how we derived the fluxes. The selected apertures are sketched in Figure 3. Apertures A-F trace extraplanar dust features while the large ellipse is used to derive global quantities. The sky background (and standard deviation) was measured from the two small elliptical apertures placed above and below the galaxy plane, not too close to the galaxy (to avoid galaxy contamination) and far from the edges of the map (to avoid unreliable fluxes due to elevated noise). The total uncertainty on the integrated photometric measurements is a combination of the error on the mean brightness in each pixel added in quadrature within the source aperture (the error map produced by *Scanamorphos*), the standard deviation of all the pixels in the background aperture, and the PACS photometer flux calibration accuracy. For the calibration uncertainties (extended sources), we adopted a large (conservative) value of 10% for both PACS and SPIRE. This value comes from adding the systematic (4-5%), statistical (1-2%), and PSF/beam size uncertainties (4%). To derive aperture corrections, we used the higher resolution image from Spitzer/IRAC 8.0 μm (McCormick et al. 2013) and measured the total flux with the same aperture employed for our analysis.

---

[2] Adapted from http://www.mrao.cam.ac.uk/~bn204/alma/python-clean.html.
[3] PACS Photometer Point Spread Function. Document PICC-ME-TN-033.
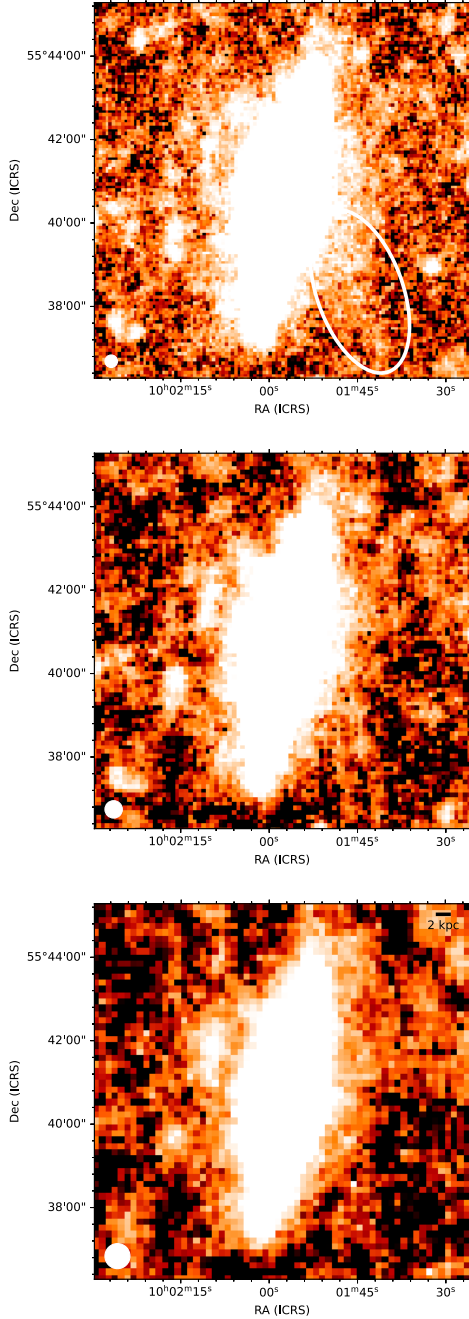
Figure 2. SPIRE 250 μm (top panel), 350 μm (middle), and 500 μm (bottom) images of NGC 3079, after processing with *Scanamorphos*. North is up and East to the left. The beam FWHM is displayed in the lower left corner of each panel. The linear scale is shown in the top right corner of the bottom panel. All panels are on an arcsinh intensity scale. The white ellipse indicates the SW filament, securely detected only in the 250 μm image.

Then we convolved the same image with the appropriate kernel to bring it to the PACS resolution[4] ([Aniano et al. 2011](#)) and remeasured the flux in the same aperture. The ratio of the unconvolved to the convolved (the same PSF as the *Herschel* PACS) flux is used as an estimate of the aperture correction. For the global flux, the big aperture resulted in small corrections with values of 1.01 and
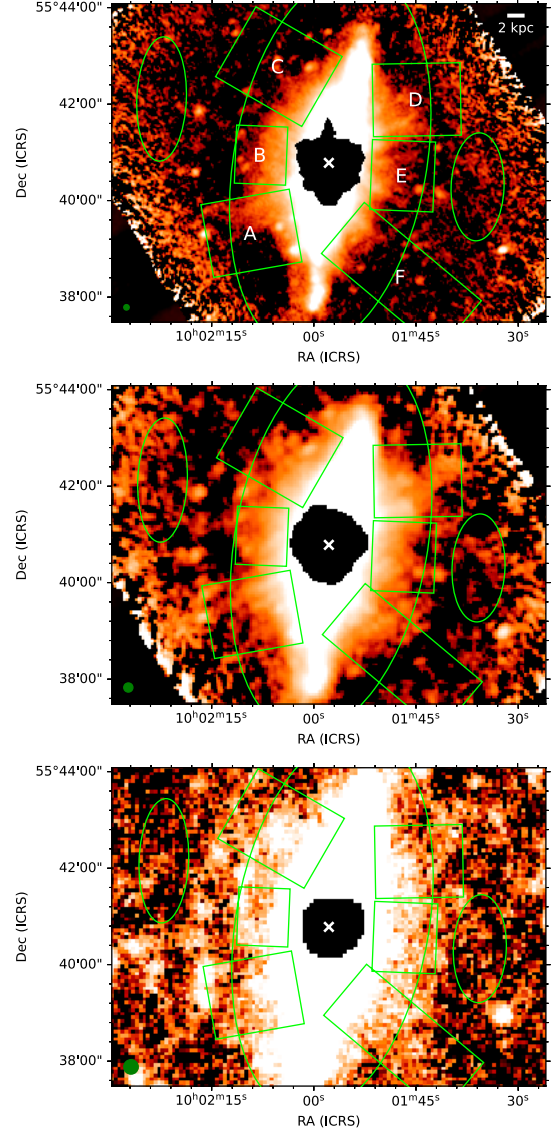
Figure 3. Extraction apertures (green boxes) used to calculate the flux densities and corresponding dust masses and temperatures in the extraplanar dust features detected in the PACS 100 and 160 μm images (top and middle panels) and SPIRE 250 μm image (bottom panel). The large ellipse is used to calculate the global values for the entire galaxy, while the small ellipses indicate the regions where the sky background was calculated. North is up and East to the left. The beam FWHM is displayed in green in the lower left corner of each panel. The linear scale is shown in the top panel. The results of this analysis are listed in Table [2](#). All panels are on an arcsinh intensity scale.

1.02 for PACS 100, and 160 μm, respectively, and 1.00 for all of the SPIRE images. We color-corrected PACS fluxes assuming a modified blackbody with $\beta = 2$ and a blackbody temperature of $T = 20$ K (0.974/0.971 at 100/160 μm).[5]

The cleaned 100 and 160 μm flux maps of Figure [1](#) were used to create the map of the S_{100}/S_{160} flux ratios presented in Figure [4](#), after convolving the 100 μm flux map to match the beam size of


Table 2. Dust Masses and Temperatures in the X-Shape Structure

Region	$f_\nu(100\,\mu m)$ (Jy)	$f_\nu(160\,\mu m)$ (Jy)	$f_\nu(250\,\mu m)$ Jy	$f_\nu(350\,\mu m)$ (Jy)	$f_\nu(500\,\mu m)$ (Jy)	T_D (K)	$\log M_d$ ($M_\odot$)
(1)	(2)	(3)	(4)	(5)	(6)	(7)	(8)
Global	109.209	119.264	47.259	19.756	7.303	23.5 ± 0.63	8.0 ± 0.04
A	0.302	0.737	0.524	—	—	16.9 ± 0.10	6.45 ± 0.02
B	0.205	0.380	0.256	—	—	18.2 ± 0.03	6.02 ± 0.01
C	0.198	0.543	0.535	—	—	15.6 ± 0.26	6.56 ± 0.04
D	0.270	0.672	0.427	—	—	17.2 ± 0.26	6.35 ± 0.04
E	0.166	0.442	0.366	—	—	16.2 ± 0.04	6.35 ± 0.01
F	0.244	0.638	0.672	—	—	15.6 ± 0.39	6.65 ± 0.08
A − F	1.384	3.412	2.775	—	—	—	7.2 ± 0.2

Column (1): Extraction aperture as defined in Fig. 3; Columns (2) − (3): Flux density at 100 and 160 μm in Jansky from the PACS data; Columns (4) − (6): Flux density at 250, 350, and 500 μm in Jansky from the SPIRE data; Column (7): Best-fit dust temperature in K; Column (8): Dust mass in solar masses derived from the best fit to the flux densities. The uncertainties on these quantities reflect the measurement errors, not the (possibly larger) systematic errors. See text for more details.
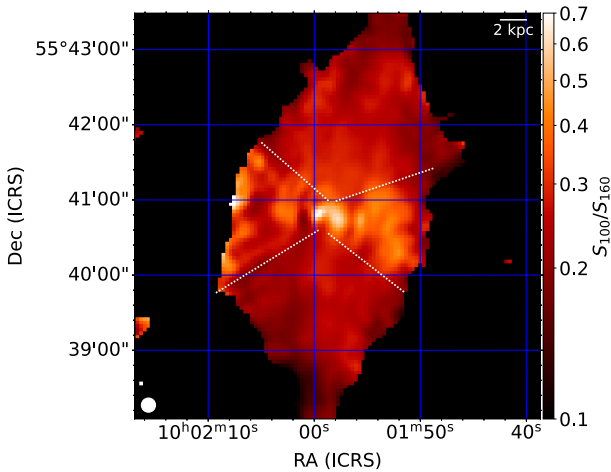
Figure 4. Ratio of the cleaned PACS 100 μm flux map to the cleaned PACS 160 μm flux map from Figure 1. North is up and East to the left. The beam FWHM is displayed in the lower left corner, while the linear scale is shown in the upper right corner. The beam size is displayed in the lower left corner. The ratios are elevated in the biconical region indicated by the white dotted lines.

the 160 μm flux map. The S_{100}/S_{160} ratios within the brighter portion of the galaxy peak in the nucleus and within a bicone aligned along the minor axis of the galaxy, coincident with the brightest X-ray emission (e.g., Strickland et al. 2004a), the double-lobed radio structure (e.g., Irwin & Seaquist 1988), and the Hα superbubbles (e.g., Veilleux et al. 1994). This is similar to the results found in both NGC 4631 (Paper I) and NGC 891 (Paper III), where the S_{70}/S_{160} ratios were found to be elevated within the X-ray brightest regions in and above the nucleus of each galaxy. It is also reminischent of the "ionization cones" seen in starburst and active galaxies (e.g., Shopbell & Bland-Hawthorn 1998; Wilson & Tsvetanov 1994; Sharp & Bland-Hawthorn 2010, and references therein). We return to this result in Section 4.2.

3.2 PACS Spectroscopy

3.2.1 [C II] 158 μm

The low-excitation atomic line [C II] 158 samples photodissociation regions (PDRs) at the interfaces between molecular, atomic,

and ionized gas phases in or near star-forming regions or AGN where intense far-ultraviolet (FUV) radiation photodissociates CO, resulting in bright emission of [O I] and [C II] (Tielens & Hollenbach 1985; Sternberg & Dalgarno 1995; Hollenbach & Tielens 1997). [C II] 158 arises from both ionized and neutral gas due to the low ionization potential (11.2 eV) needed to create C$^+$. The relatively high second ionization potential (24.4 eV) needed to ionize C$^+$ means that C$^+$ is often the dominant atomic species of carbon. [C II] 158 is the dominant coolant in regions with densities $n_H \sim 10 - 10^5$ cm^{-3} and temperatures $T \sim 100 - 300$ K, and is the strongest emission line from cooler gas ($T < 10^4$ K) in galaxies (Carilli & Walter 2013).

A signal-to-noise ratio map of the [C II] 158 line emission in NGC 3079 is presented in Figure 5a, where the largest SNRs are observed in the nucleus with values exceeding ~ 50. The velocity-integrated [C II] 158 emission-line flux map is shown in Figure 5b. The [C II] 158 line emission in NGC 3079 is diffuse and elongated along the direction of the major axis of the (inner) disk, which runs along P.A. $\simeq 165°$. Figures 5c and 5d present the kinematics of the [C II] line-emitting gas. The velocities and widths of the [C II] 158 emission line profiles in each spaxel are described using a non-parametric method based on interpercentile range measurements. v_{50} is the median velocity of the fitted emission line profile, i.e. 50% of the emission is produced at velocities below v_{50}. Zero velocity corresponds to the rest wavelength at the systemic velocity of NGC 3079. $W_{1\sigma}$ is the width of the line profile within 1-σ standard deviation of v_{50} (i.e. encompassing $\sim 68\%$ of the total line flux). The values of [C II] 158 v_{50} range from ~ -120 to $\sim +160$ km s^{-1} and indicate that the gas on the N side is approaching us while the gas on the S side is receding from us, consistent with disk rotation traced by the warm-ionized, neutral-atomic, and molecular gas (Veilleux et al. 1999; Koda et al. 2002; Yamauchi et al. 2004; Shafi et al. 2015). The line widths peak in the center and along the kinematic minor axis of the disk i.e. along the same direction as the ionized and relativistic outflow in this system. A more detailed interpretation of these data is postponed until Section 4.2, where the effects of beam smearing and instrumental broadening are taken into account.

3.2.2 OH 119 μm

We focus our attention on the ground-state OH 119 μm $^2\Pi_{3/2} J = 5/2 - 3/2$ rotation Λ-doublet. This feature is the strongest transition in
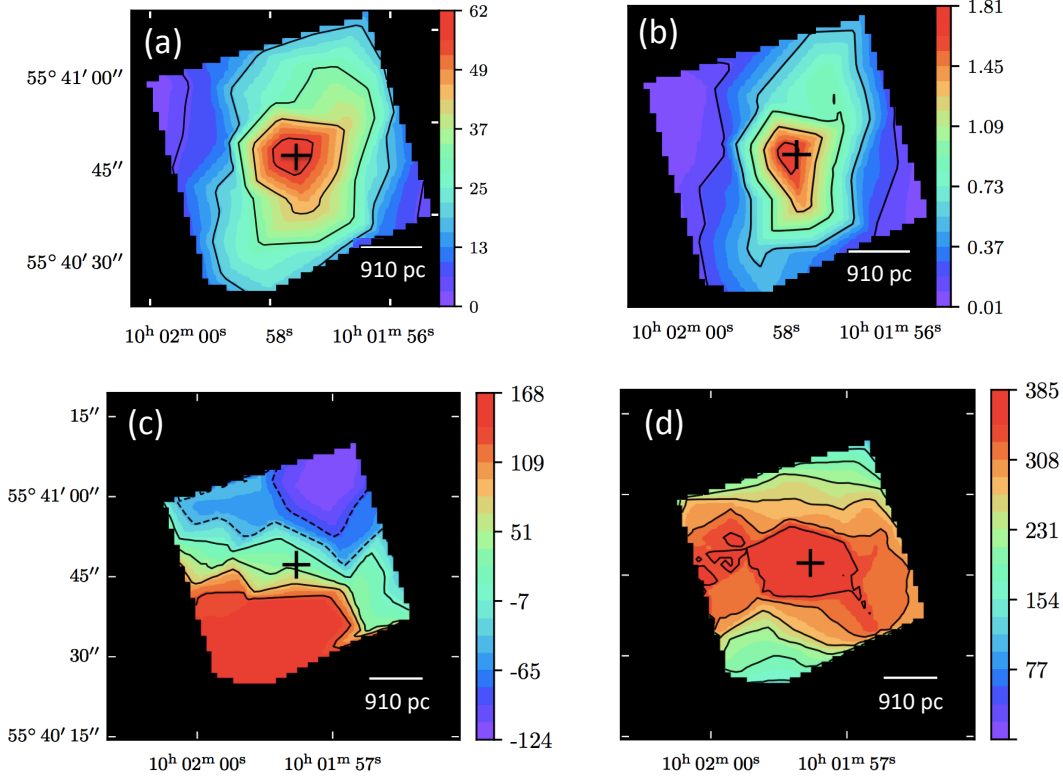
Figure 5. (a) Signal-to-noise map of [C II] 158 in NGC 3079. Contours are 0.1, 0.3, 0.5, 0.7, 0.8, and 0.9 of the peak value. The black cross in this and the other panels marks the adopted galaxy center. (b) Total integrated emission line fluxes in 10^{-17} W m^{-2}. Contours are 0.1, 0.3, 0.5, 0.7, and 0.9 of the peak flux. (c) Map of the median velocities, v_{50}, in km s^{-1}. Contours are in eight equal steps between the minimum and maximum velocities. (d) Map of the 1-σ line widths, $W_{1\sigma}$, in km s^{-1}. Contours are 0.4, 0.5, 0.6, 0.7, 0.8, and 0.9 of the peak width. North is up and East to the left. The linear scale is shown in each panel.

NGC 3079 and is positioned near the peak spectroscopy sensitivity of PACS. OH 119 is a sensitive tracer of the molecular gas. It is mainly excited through absorption of far-IR photons and selectively traces a region close to the central source of strong far-IR radiation density.

We characterize the OH line profiles in the same manner as the [C II] emission line (i.e. using v_{50} and $W_{1\sigma}$). The results are summarized in Figure 6. Panel (a) of this figure shows the PACS IFU footprint (black lines and squares) and the outline of the region characterized with anomalously high [C II] 158 line widths (white line; discussed in Sec. 4.2) overlaid on the 22 μm WISE image of NGC 3079. Panel (b) shows the spline fits to the continuum in each spaxel, all on the same flux scale, while panel (c) presents the fits to the continuum-subtracted line profile, adjusted to best show the results. Finally, panel (d) shows maps of the line profile properties for the absorption and/or emission components fitted to the spectra. The 1-σ line width maps have not been corrected for instrumental broadening.

It is clear from panels (b) and (d) in Figure 6 that OH is largely seen only in absorption and is concentrated in the inner $3 \times 3 \times 9\farcs4$ grid of the data cube, or $\sim 3 \times 3$ kpc centered on the nucleus. The OH line emission is not securely detected in this galaxy, thus the corresponding Gaussian fits shown in panels (c) and (d) of Figure 6 are unconstrained. The $N - S$ 280 km s^{-1} velocity gradient traced by [C II] 158 is not visible within the inner 3×3 grid where OH absorption is strongly detected. The OH profiles in this region are uniformly broad with $W_{1\sigma} \simeq 350 - 450$ km s^{-1}. These widths are similar to those of the [C II] emission line profiles in the same region. We return to these results in Section 4.2.

4 DISCUSSION

### 4.1 X-Shape Dust Structure

4.1.1 Dust Masses

The dust masses were estimated by assuming a simple single-temperature modified black body (MBB) to the infrared SED using

$$F_\nu = \frac{M_d \kappa_\nu B_\nu(T_d)}{d^2}. \tag{1}$$

Here M_d is the dust mass, B_ν is the Planck function, T_d is the dust temperature, d is the distance to the galaxy, and κ_ν is the dust emissivity, $\kappa_\nu = \kappa_0(\nu/\nu_0)^\beta$, where κ_0 is the dust opacity at 350 μm. We follow the same procedure as in Papers I-III, choosing $\kappa_0 = 0.192$ m^2 kg^{-1} and $\beta = 2$, and leaving the dust temperature T_d as a free parameter. This value of the dust opacity is based on the best fit to the average far-infrared dust emissivity for the Milky Way model presented in Draine (2003), which yields a best-fit spectral index value of $\beta = 2.0$.

The resulting dust masses and temperatures are listed in Table 2. The detection of extraplanar emission at 250 μm in apertures A-E is uncertain so the dust masses derived within these apertures, 1.2×10^7 $M_\odot$, should be considered upper limits. The dust mass in aperture F, where extraplanar 250 μm emission is securely detected, provides a robust lower limit of $\sim 4 \times 10^6$ $M_\odot$ for the total dust mass in the X-shape structure. In the following discussion, we use (4 $- 16) \times 10^6$ $M_\odot$ as the most plausible range of values for the dust mass in the overall extraplanar structure.
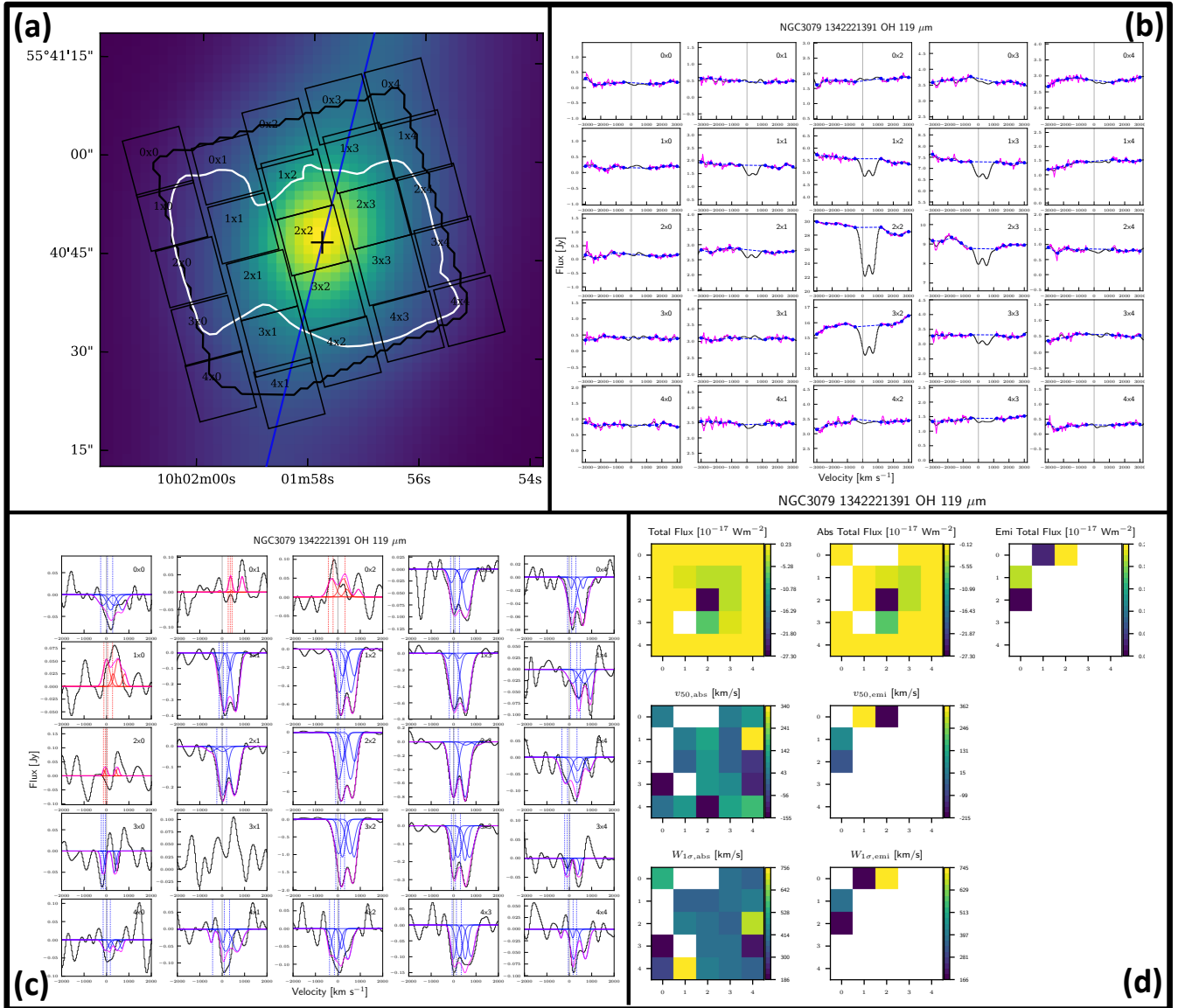
Figure 6. (a) PACS IFU footprint of OH 119 (black squares) overlaid on the 22 μm WISE image of NGC 3079. North is up and East to the left for this and all other panels in this figure. The white contour marks the spatial extent of the high-$W_{1\sigma}$ [C II] 158 region (defined in Section 4.2.3). The black contour outlines the PACS footprint of the [C II] 158 observation. The black cross marks the adopted galaxy center and the blue line marks the galaxy major axis. (b) Spline fits to the OH 119 continuum (blue dashed lines). Black lines are the observed data. Magenta areas indicate the regions used to fit the continuum. Blue dots mark the pivot points used to fit the spline. (c) Line profile fitting results of the continuum-subtracted spectra. Solid blue (red) lines indicate Gaussian absorption (emission) components. Vertical dashed blue (red) lines mark the v_{16}, v_{50}, and v_{84} velocities in absorption (emission). (d) Top row, from left to right shows the total velocity-integrated flux of the fitted OH line profiles, the total flux in the absorption components only, and the total flux in the emission components only. Middle row shows v_{50} for the absorption (left) and emission components (right). Bottom row shows the $1-\sigma$ line widths of the absorption (left) and emission (right) components. OH line emission is not securely detected in this galaxy.

4.1.2 Multiwavelength Comparisons

Figures 8, 9, and 10 compare the far-infrared PACS and SPIRE emission of NGC 3079 with the deep *GALEX* and *XMM-Newton* data recently analyzed by Hodges-Kluck et al. (2020). There is an excellent match between the far-infrared X-shape structure and the base of the biconical outflow visible in the far-ultraviolet and soft X-ray maps. This X-shape structure has also been detected at Hα (Figs. 7 and 5 in Heckman et al. 1990; Veilleux et al. 1995, respectively). These results suggest that the far-infrared X-shape structure is physically associated with the large-scale galactic wind

of NGC 3079. In this picture, dusty material originally in the galactic disk of NGC 3079 is lifted above the disk and entrained in the large-scale galactic wind.

4.1.3 Implications on the Energetics

The energy needed to lift the dusty material making up the X-shape structure may be derived following the same procedure as that used in Papers I and III. First, we need to estimate the total (gas + dust) mass associated with the extraplanar dust. Here, it is important
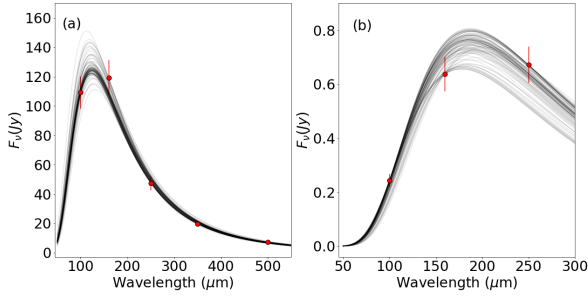
Figure 7. Fits to the far-infrared energy distribution of (a) the global fluxes from NGC 3079, (b) the fluxes measured in Aperture F as defined in the top panel of Fig. 3.

to account for all possible gas phases, which is challenging. The amount of hot ionized material associated with the base of the X-ray emitting filaments, $\sim 4 \times 10^7 \, M_\odot$ (from Table 1 of Hodges-Kluck et al. 2020, excluding the central region), implies a ratio of the hot ionized gas mass to the dust mass of $3 - 10$, which is a hard lower limit on the total gas-to-dust mass ratio. On the other hand, the amount of warm ionized gas in the X-shape Hα structure remains unknown; Hα is not only very faint but the large uncertainties on the 3D geometry on the Hα filaments (e.g., cylinders *versus* conical walls in projection) make it difficult to derive a reliable gas density in this structure from the Hα emission (typical line ratio diagnostics such as the [S II] $\lambda6731/\lambda6716$ cannot be used in this low-density regime). While cooler gas no doubt also contributes to increasing the gas-to-dust mass ratio, there is no report at present of extraplanar molecular gas on the scale of the X-shape structure (e.g., Sofue & Irwin 1992). Finally, extraplanar H I gas has been detected in NGC 3079 (see Fig. 1 in Shafi et al. 2015), but there is no obvious overlap between the H I emission and the X-shape structure down to a sensitivity level corresponding to an H I column density of $\sim 0.05 \times 10^{20}$ cm^{-2}.

In the end, given the large uncertainties on the derivation of the gas-to-dust mass ratio in the X-shape structure, we make the simplifying assumption that the gas-to-dust ratio of the X-shape structure is similar to that of the disk ISM, i.e. it has not been modified by the entrainment in the wind. We return to the validity of this assumption below (Sec. 4.1.4). In that case, a Galactic dust-to-gas mass ratio of $100 - 150$ (e.g., Draine et al. 2007) implies a gas mass of $(4 - 24) \times 10^8 \, M_\odot$. On the other hand, Yamagishi et al. (2010) derived a gas-to-dust mass ratio of ~ 860 for NGC 3079 as a whole and ~ 1100 within the central (2 kpc radius) region. If these unusually high gas-to-dust mass ratios also apply to the extraplanar material, then the gas mass in the X-shape structure would be up to $(3 - 18) \times 10^9 \, M_\odot$.

We have reexamined this question using our *Herschel* data and fitting the global far-infrared SED of NGC 3079 with a single-temperature MBB, $\kappa_0 = 0.192$ m^2 kg^{-1}, and $\beta = 2$, as we did for the X-shape structure. The results are listed on the first line of Table 1 and shown in the left panel of Figure 7. The flux measurements are consistent with other published values from shallower data (Meléndez et al. 2014; Shimizu et al. 2016). The derived total dust mass of $1.0 \times 10^8 \, M_\odot$ is $\sim 5 \times$ higher than the value adopted by (Yamagishi et al. 2010, scaled to our adopted distance of 19 Mpc). The global gas-to-dust mass ratio we derive from our data, using an updated total (molecular + atomic) gas mass of $2 \times 10^{10} \, M_\odot$ (combining the

values from Devereux & Young 1990; Sofue & Irwin 1992; Irwin et al. 1987; Shafi et al. 2015), is 200. Using this range of gas-to-dust ratios for our calculation of the gas mass in the X-shape structure, we get $(8 - 32) \times 10^8 \, M_\odot$. Interestingly, note also that the best-fit dust temperature (24 K) to the global SED is higher than that of the X-shape filaments. We return to this issue below (Sec. 4.1.4).

Following Papers I and III, we estimate the energy needed to lift this material up to a height z above the mid-plane of the galaxy by assuming an isothermal sheet model for the vertical distribution of light and mass in galactic disks (Howk & Savage 1997):

$$\begin{aligned} \Omega \quad = \quad & 1 \times 10^{56} \text{ ergs} \left(\frac{M}{10^9 M_\odot} \right) \left(\frac{z_o}{700 \text{ pc}} \right)^2 \left(\frac{\rho_o}{0.185 \text{ M}_\odot \text{ pc}^{-3}} \right) \\ & \times \ln \left[\cosh \left(\frac{z}{z_o} \right) \right], \end{aligned} \quad (2)$$

where ρ_o is the mass density at the midplane, M is the mass of lifted material, and z_o is the mass scale height of the stellar disk. Here we use a mass scale height for the stellar disk of 380 pc, derived at ~ 2 μm (Veilleux et al. 1999), and ignore the well-known boxy, peanut-shaped bulge in this object (Veilleux et al. 1999, and references therein) since we are only concerned with the large-scale X-shape filaments which are not affected by the inner bulge. Assuming an average mid-height for the X-shape structure above the plane of about 3 kpc, and a starting point at $z = z_0 = 380$ pc, then the gain in potential energy is:

$$\Delta\Omega = 1 \times 10^{56} \text{ ergs} \left(\frac{M}{10^9 M_\odot} \right) \left(\frac{\rho_o}{0.097 \text{ M}_\odot \text{ pc}^{-3}} \right). \quad (3)$$

Note the rather weak dependence on the starting point: if the material starts at a distance ten times closer to the mid-plane, $z = 0.1 \, z_0 = 38$ pc, then the energy needed to lift the material would be only $\sim 1.05 \times$ higher (note that eqn 2 is undefined at the mid-plane). The same cannot be said about the average mid-height for the X-shape structure: a value of 1 kpc instead of 3 kpc gives $\Delta\Omega = 0.13 \times 10^{56}$ ergs. Another uncertainty on the prediction of the potential energy comes from the mass density at mid-plane, where we adopted a value of 0.097 M$_\odot$ pc^{-3}, representative of the total mass density at the solar position (see Bland-Hawthorn & Gerhard 2016, for details). This is probably a good first-order approximation since NGC 3079 and the Milky Way share similar morphological, kinematic, and dynamical properties (Veilleux et al. 1999).

This gain in potential energy is large, the equivalent of about 10^5 supernova explosions, and larger than the kinetic energy of the nuclear Hα line-emitting bubble, $(0.5 - 6) \times 10^{55} \sqrt{f}$ ergs, regardless of the gas filling factor f (< 1; Cecil et al. 2001, for $d = 19$ Mpc). This last comparison is not completely fair since the nuclear bubble extends only on kpc scale while the infrared filaments reach distances of up to 25 kpc. The dynamical time scale of the nuclear bubble is $\sim 10^6$ yrs (Cecil et al. 2001), while the filaments were likely produced over a much longer time scale. For instance, the lifetime of the 60-kpc galactic wind reported in Hodges-Kluck et al. (2020) is estimated to be 120 Myr, two orders of magnitude larger than the bubble time scale. Using a AGN jet power of $\sim 6 \times 10^{41}$ erg s^{-1} from Shafi et al. (2015), adjusted for $d = 19$ Mpc, which accounts for the various methods that can be used to convert radio luminosities into jet power, the energy needed to lift the X-shape structure would require the jet to inject 50% of its kinetic energy and remain turned on for $\sim 10^7$ years. This time scale is long but not unreasonable: for instance, the buoyancy time scale of the radio
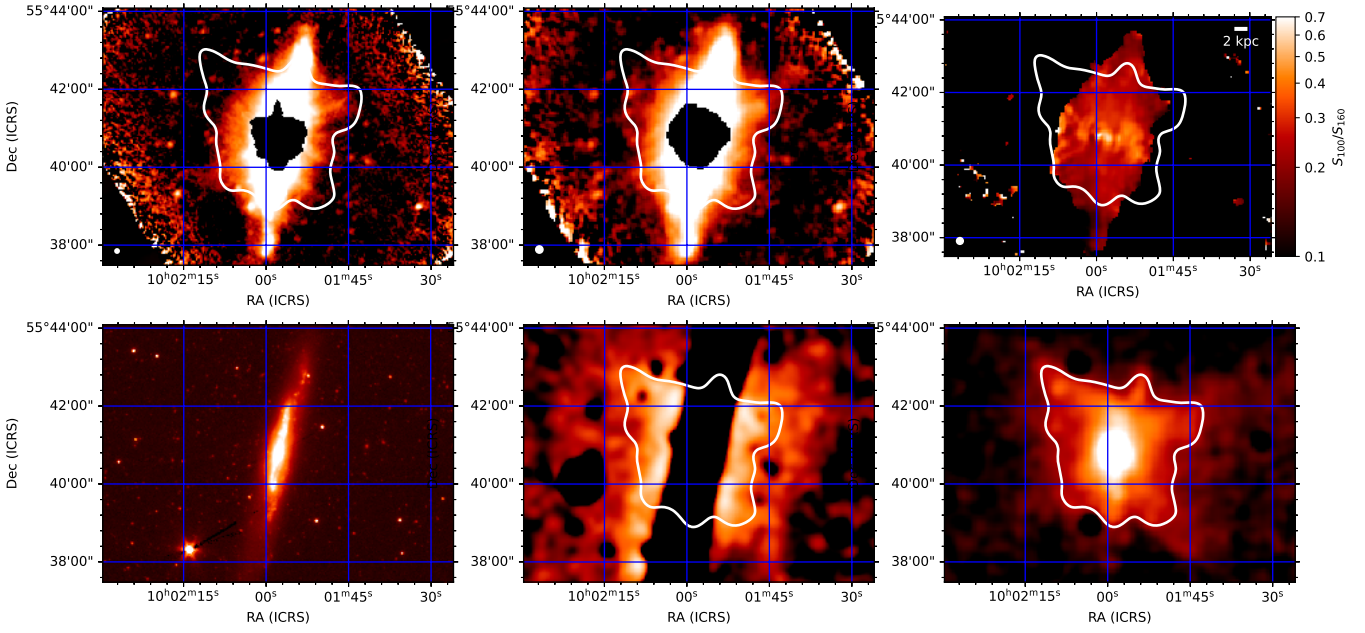
Figure 8. Multi-wavelength comparison. (top left) PACS 100 μm map. (top center) PACS 160 μm map. (top right) PACS 100-to-160 μm flux ratio map. The beam FWHM is displayed in the lower left corner of each panel. (bottom left) IRACS 4.5 μm image, (bottom center) FUV map from Hodges-Kluck et al. (2020), (bottom right) *XMM-Newton* X-ray map from Hodges-Kluck et al. (2020). The white contour in the various panels shows one of the X-ray isophotes for comparison. North is up and East to the left. The linear scale is shown in the upper right panel. All panels are on an arcsinh intensity scale.
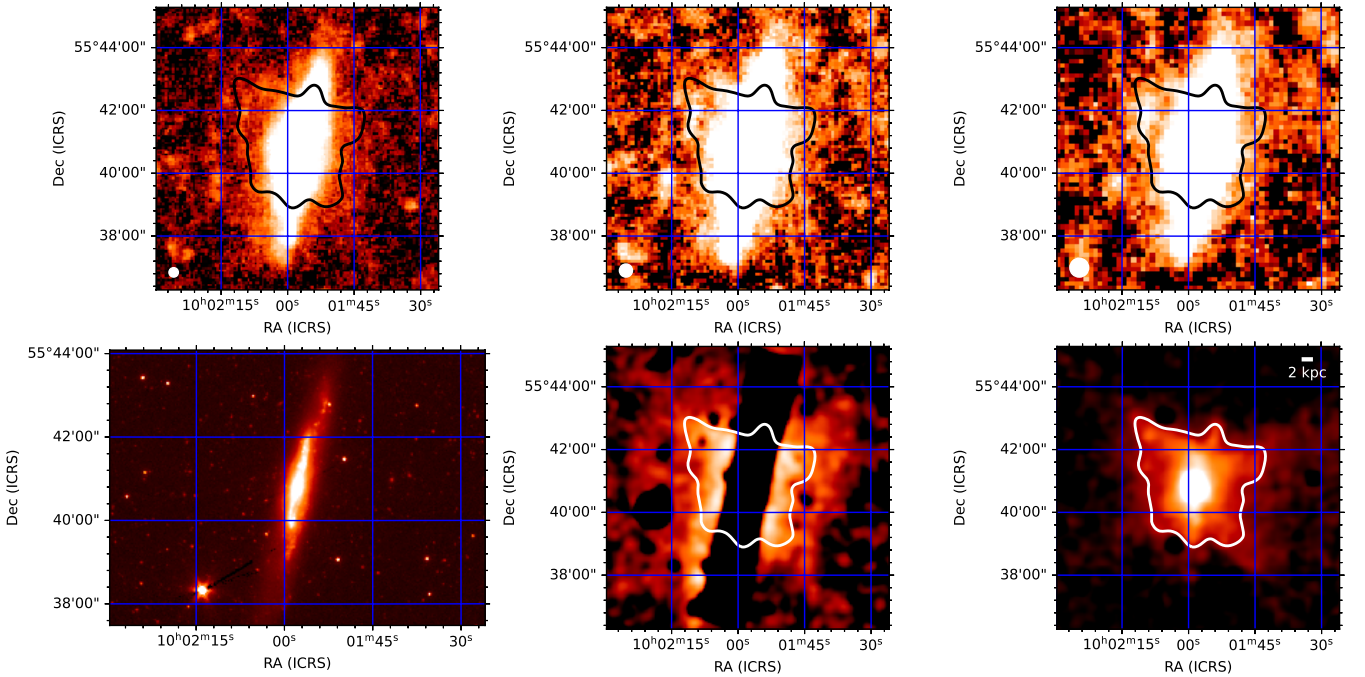
Figure 9. Multi-wavelength comparison. (top left) SPIRE 250 μm map. (top center) SPIRE 350 μm map. (top right) SPIRE 500 μm map. The beam FWHM is displayed in the lower left corner of each panel. (bottom left) IRACS 4.5 μm image, (bottom center) FUV map from Hodges-Kluck et al. (2020), (bottom right) *XMM-Newton* X-ray map from Hodges-Kluck et al. (2020). North is up and East to the left. The white contour in the various panels shows one of the X-ray isophotes for comparison. North is up and East to the left. The linear scale is shown in the lower right panel. All panels are on an arcsinh intensity scale.
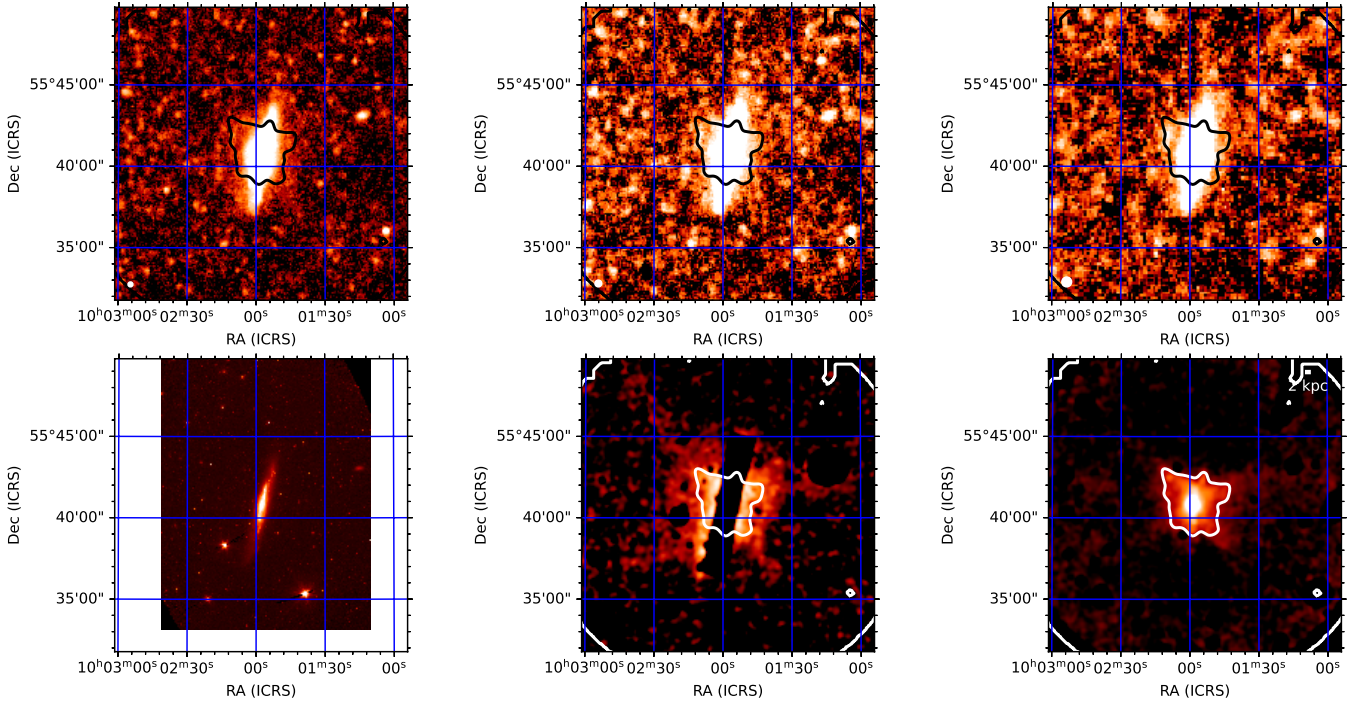
Figure 10. Same as Figure 9 but showing a larger field of view. (top left) SPIRE 250 μm map. (top center) SPIRE 350 μm map. (top right) SPIRE 500 μm map. The beam FWHM is displayed in the lower left corner of each panel. (bottom left) IRACS 4.5 μm image, (bottom center) GALEX FUV map from Hodges-Kluck et al. (2020), (bottom right) *XMM-Newton* X-ray map from Hodges-Kluck et al. (2020). The white contour in the various panels shows one of the X-ray isophotes for comparison. North is up and East to the left. The linear scale is shown in the lower right panel. All panels are on an arcsinh intensity scale.

structure in NGC 3079 has been estimated to be also $\sim 10^7$ yr (Cecil et al. 2001).

In this mass-loaded AGN-driven wind scenario, the AGN injects material in the ISM at a rate of $\sim L_{\rm kin}/(\frac{1}{2} V_{\rm wind}^2)$, where $V_{\rm wind}$ is the AGN wind velocity at the source and the AGN wind kinetic power $L_{\rm kin}$ needs to average out to at least $\sim 50\%$ of the AGN jet power, or $\sim 3 \times 10^{41}$ erg s^{-1}, for a period of $\sim 10^7$ years to be able to lift the dusty material into the halo. This mass outflow rate is only $0.01 - 1 \, M_\odot$ yr^{-1} for $V_{\rm wind} = 1000 - 10,000$ km s^{-1}, more than 2-4 orders of magnitude smaller than the time-averaged mass ejection rate derived by dividing the inferred gas mass in the X-shape structure by 10^7 yrs. In the pure-starburst scenario, which we consider less likely, the starburst injects material in the ISM at a rate ~ 0.26 SFR (Veilleux et al. 2005), where SFR $< 2.6 \, M_\odot$ yr^{-1} (Yamagishi et al. 2010), or about two orders of magnitude smaller than the above time-averaged mass ejection rate into the halo. Thus, regardless of the nature of the wind energy source (AGN or starburst), the implied large mass-loading factor (defined as the rate of mass ejected into the halo divided by the mass outflow rate produced at the source) adds support to the idea that most of the dust in the halo originates from disk material being mass-loaded into the wind. Taken at face value, these mass-loading factors are considerably larger than those predicted by numerical simulations of isolated galaxies (Hopkins et al. 2012). However, caution should be exercised when interpreting these results since the derived mass-loading factors are only order-of-magnitude estimates and the simulations are idealistic in the sense that they do not include a realistic hot coronal gas component or intergalactic medium.

So far, our discussion has focused on the necessary (minimum) condition of lifting the material into the halo. In addition, we also

need to take into account the work done against the surrounding ISM and CGM. A shell that moves faster than the sound speed will accelerate as it breaks through the disk. Rayleigh-Taylor instabilities will disrupt the shell and a free-flowing galactic wind will develop (Chevalier & Clegg 1985). The critical rate of energy injection for blowout to occur depends on the vertical gas density distribution. Using equation (5) of Strickland et al. (2004b) (or, equivalently, equation (2) in Paper III), the critical mechanical power to break out through the thick H I disk of NGC 3079 is

$$L_{\rm crit} = 10^{38} \text{ ergs s}^{-1} \left(\frac{0.1 \text{ cm}^{-3}}{n_0} \right)^{1/2} \left(\frac{P_0/k}{10^4 \text{ K cm}^{-3}} \right)^{3/2} \left(\frac{H}{\text{kpc}} \right)^2 \tag{4}$$

where we have assumed that the vertical gas density profile of the thick disk of NGC 3079 follows approximately an exponential distribution with a scale height $H = 1$ kpc and central gas density $n_0 = 0.1$ cm^{-3} (Irwin & Seaquist 1991, using $d = 19$ Mpc). The rate of energy injection from the AGN jet in NGC 3079 ($\sim 6 \times 10^{41}$ erg s^{-1}) exceeds this breakout criterion by a factor >1000. The energy injection rate also exceeds the critical rate to break out of the thin molecular disk (Sofue et al. 2001; Koda et al. 2002) and thick warm-ionized gas layer (Veilleux et al. 1995).

This picture of a powerful, long-lived AGN-driven outflow that breaks out from the disk can also naturally explain the large-scale X-shape morphology seen in the far-infrared, UV, and X-rays. The breakout flow is expected to be a strong function of polar angle as seen from the nucleus (Cecil et al. 2001). Neglecting the CGM, the flow expands freely along the minor axis, but at some critical angle its ram pressure becomes comparable to the thermal pressure in the

diffuse component of the ISM; at larger angles a standing bow shock in the galaxy disk decelerates and deflects wind around a region of undisturbed ISM gas. The wind subsequently reaccelerates into the halo. In the disk plane itself, the flow compresses the ISM to form a standing "ring" shock at $r \simeq 800$ pc. Cecil et al. (2001) have argued that the linear X-shape Hα filaments join the galaxy disk at radii of $\sim$ 800 pc, forming a "concave bowl" in the *HST* images that coincides with the standoff outer disk shock / contact-discontinuity between the shocked wind and the unperturbed ISM (see their Figs. 10 and 12 for instance). Unfortunately, the limited angular resolution of the *Herschel* data, combined with the uncertainties associated with removing the PSF from the PACS images, prevent us from tracing the X-filaments of the far-infrared structure inside of $\sim$ 2-3 kpc and determining whether the match between the far-infrared and Hα filaments continues down to the nuclear scale.

The actual situation in NGC 3079 is undoubtedly more complicated: interaction with the CGM will slow down the free-flowing wind, perhaps allowing it to cool and form a galactic fountain rather than escape the gravitational potential. Equation 4 cannot be used to estimate the critical mechanical power needed to break out through the CGM as it neglects gravity, radiative losses, and the density profile of the CGM (see Lochhaas et al. 2018, for examples of semi-analytic models of starburst-driven winds).

4.1.4 Dust Entrainment and Survival

Several processes may destroy the dust entrained in the outflow (e.g., Galliano et al. 2018; Veilleux et al. 2020): collisions with other grains, sputtering due to collisions with ions, sublimation or evaporation, explosion due to ultraviolet radiation, and alteration of grain material by cosmic rays and X-rays. A distinction is often made between thermal sputtering, where the sputtering rate only depends on the local gas properties (namely n_H and T), and non-thermal (inertial) sputtering, where the dust-gas relative velocity is a crucial parameter. The thermal sputtering timescale is

$$t_{\mathrm{sput}} \simeq 3.3 \times 10^3 \left(\frac{a}{0.1\ \mu m} \right) \left(\frac{n_H}{10\ \mathrm{cm}^{-3}} \right)^{-1} \mathrm{yr}, \qquad (5)$$

for 10^6 K $\lesssim T \lesssim 10^9$ K, and increases dramatically below $\sim 10^6$ K (Nozawa et al. 2006; Hu et al. 2019). Assuming the hot ($T \simeq 0.35$ keV $= 4 \times 10^6$ K), low-density ($n_H \simeq 10^{-3}$ cm^{-3}), X-ray emitting material in the X-shape filaments reported by Hodges-Kluck et al. (2020) is in contact with the dust would imply a thermal sputtering timescale of 3×10^7 yrs for dust grains with $a = 0.1\ \mu$m, similar to the duration of the AGN jet cycle needed to produce the X-shape structure.

The presence of dust in the X-shape filaments would seem to exclude shocks faster than ~ 300 km s^{-1}, which would rapidly destroy the dust through non-thermal (inertial) sputtering (e.g., Arendt et al. 2010; Lakićević et al. 2015; Temim et al. 2015; Dopita et al. 2016), although the presence of dust behind the reverse shock in some supernova remnants (e.g., Kochanek 2011; Matsuura et al. 2019) and in galaxies in general (Gall & Hjorth 2018) suggests that dust is either more resilient than originally predicted (e.g., Silvia et al. 2010; Biscaro & Cherchneff 2016) or it reforms rapidly behind the shocks (Humphreys et al. 2012; Seale et al. 2012; Gall et al. 2014), despite models predicting the contrary (e.g., Biscaro & Cherchneff 2014).

Hodges-Kluck et al. (2020) argued that shocks with velocities exceeding 500 km s^{-1} are needed to produce the large-scale X-ray filaments if the X-rays come from cool material shock-heated

by the wind. To survive, the dust must be shielded from these fast shocks, and the low dust temperature coincident with these filaments ($\sim$15 K, compared to 25 K in the disk) indicates that the only heat source is radiation leaking out of the disk. This is also consistent with the interpretation that the extraplanar FUV and NUV light at low latitudes is reflected by dust in these filaments, and indeed the diffuse UV light is brightest in the same region where the X-ray filaments are brightest. The presence of the dust raises the possibility that the hot gas is not primarily shock heated, but instead traces disk material mass-loaded into the wind that has mixed with a hotter phase (as envisioned in Cooper et al. 2008). The wind is sufficiently mature that this is a strong possibility, as any terminal shock is at least 60 kpc away. In this case, the density and temperature do not map straightforwardly to the wind speed, and the thermal sputtering timescale (or cloud evaporation timescale) is the most appropriate one for grain survival.

4.2 Cool Nuclear Outflow

In Section 3.2, we showed that the [C II] 158 velocity field of NGC 3079 is dominated by the rotational motion of the gas in the disk, while that of the OH absorption feature is not. However, in both cases, the profiles near the center are broad ($W_{1\sigma} = 350 - 450$ km s^{-1}), suggestive of a turbulent medium. To more quantitatively assess the influence of the nuclear outflow on the kinematics of [C II] 158 line profiles, we need to remove the instrumental effects associated with the finite spectral and spatial resolutions of the data and examine the residuals. This is a multi-step process which is detailed here.

4.2.1 Beam Smearing

An important aspect of deriving accurate galaxy kinematics from velocity fields is to take into account the effect of beam smearing (Bosma 1978). The radial velocities in a galaxy vary on spatial scales smaller than the beam size of the observing instrument. Effectively, this means that the velocities at different radii will be blended, thus flattening the observed velocity field gradient, decreasing the slope of the derived rotation curve at the galaxy center, and broadening the width of the observed line profiles. This is a significant problem since the broadening effect can be incorrectly attributed to intrinsic gas velocity dispersion.

Fortunately, we can employ methods that utilize the full 3D data cube (two spatial dimensions and one spectral dimension) of the galaxy and build a model that directly incorporates the instrument 2D point spread function and spectral resolution. To do this we use the software package ^{3D}BAROLO[6] (Di Teodoro & Fraternali 2015) which simulates the observational data in a cube by building a "tilted-ring" model that best fits the data. Accounting for the instrumental contribution to the observed data will result in a disk model which more accurately captures the true kinematics of the gas. The details of the "tilted-ring" model and the employment of ^{3D}BAROLO are discussed in the following section.

4.2.2 Tilted Ring Model

The velocity field of a disk galaxy can be described by a "tilted-ring" model (Rogstad et al. 1974), where the disk is built from a series of concentric annuli of various radii. This model assumes that the line

---

6 http://editeodoro.github.io/Bbarolo/, version 1.4

emitting material is confined to a thin disk and that the kinematics are dominated by rotational motion. Emission of the gas in each ring is described by geometric parameters (centroid, radius, width, scale height, inclination angle along the line of sight of the observer, and position angle of the major axis) and kinematic parameters (systemic velocity, rotational velocity, and velocity dispersion). For ^{3D}ʙᴀʀᴏʟᴏ, the instrumental spectral and spatial resolutions are also inputs so that the final model accounts for both instrumental effects.

In reproducing the observed data cube, ^{3D}ʙᴀʀᴏʟᴏ assumes that all of the velocity dispersion is due to rotation and turbulence. Given that an outflow may exist along the minor axis of NGC 3079, this assumption means that the velocity dispersion of the disk model will be overestimated, with the largest errors at the center of the galaxy where line broadening suffers the most from beam smearing.

We attempt to mitigate this effect by assuming a constant velocity dispersion across the disk and estimate the value of this velocity dispersion using data outside the galaxy center where beam smearing is the least severe. The data are fit in two stages. In the first stage, the gas velocity dispersion and the rotational velocity are left as free parameters. The remaining parameters are input as "correct" values and held constant. Afterwards, the mean of the fitted gas velocity dispersions of the three outermost rings is then computed. For the second stage, this mean dispersion is input as a fixed parameter and only the rotational velocity is left free. The resultant disk model is the assumed galaxy velocity field.

4.2.3 Defining the Impact of the Outflow

Any potential impact of the outflow on the [C II] kinematics may be delineated from those of the disk by examining the residuals in v_{50} and in $W_{1\sigma}$ between the observed data and the modeled disk (Δv_{50} and $\Delta W_{1\sigma}$, respectively). Recall from Section 4.2.2 that the modeled galaxy velocity field accounts for the instrumental spatial and spectral resolutions. Therefore, in the residuals, the instrumental effects have been removed. Experimentation on *Herschel* PACS data of other galaxies with known spatially resolved outflows along their minor axes, including M 82 (Contursi et al. 2013), has shown that the excess line widths are a more reliable indicator of the outflow than the v_{50} residuals, which are more directly affected by common dynamical features in disk galaxies, such as spiral arms, nuclear bars, and warped disks (Stone 2020). This is also true for NGC 3079 which hosts a weak bar that influences the kinematics of the gas in the central $\sim 10''$ region (e.g., Veilleux et al. 1999; Koda et al. 2002).

While $\Delta W_{1\sigma}$ is a more robust tracer of outflows than Δv_{50}, the impact on $\Delta W_{1\sigma}$ from non-circular motions in the gas around spiral arms, stellar bars, and disk warps cannot be ignored. Therefore, when defining the spatial location of the wind, it is important to explore different minimum thresholds in $\Delta W_{1\sigma}$ which would account for gas motions not related to the outflow. The results for two thesholds, $\Delta W_{1\sigma} > 25$ km s^{-1} and $\Delta W_{1\sigma} > 50$ km s^{-1}, are shown in Figure 11. Our experimentation on other galaxies with known spatially resolved outflows indicates that the smaller of these two velocity thresholds already minimizes the inclusion of regions where the excess line widths are spatially coincident with spiral arms, stellar bars, and disk warps in the central regions where the outflows are located (Stone 2020). While the higher velocity threshold does more effectively exclude gas motions unrelated to the outflows, such a threshold has a tendency to exclude a large portion of [C II] outflows altogether, as in the case of M 82 (Contursi et al. 2013). We therefore favor the lower of these two line width thresh-

olds although, as shown in Figure 11, the results of our analysis in NGC 3079 are not sensitive to this threshold value.

4.2.4 Wind Kinematics and Multiwavelength Comparison

The [C II] 158 v_{50} residuals in the wind region (Fig. 11a, Columns 4-5) do not show any regular pattern. In contrast, the [C II] 158 $\Delta W_{1\sigma}$ map (Fig. 11b, Column 4-5) shows a clear E-W elongated feature with $\Delta W_{1\sigma} \gtrsim 100$ km s^{-1}, about $10''$ in length and off-centered to the SE from the nucleus. The contour marking $\Delta W_{1\sigma} \sim 75$ km s^{-1} delineates a more extended E-W structure that encompasses this elongated high-$\Delta W_{1\sigma}$ feature.

A comparison of the [C II] 158 line profiles with those of CO (1-0) (e.g., Figure 9 of Koda et al. 2002) indicates that the [C II] 158 line-emitting gas is largely unaffected by the bar streaming and spiral arm disturbances detected in the kinematics of the molecular gas. We see no obvious match in our data with the double-peaked CO (1-0) profiles observed SE and NW of the nucleus in the data of Koda et al. (2002). Moreover, [C II] 158 Δv_{50} and $\Delta W_{1\sigma}$ extend further ($>10''$) and along a different orientation (E-W) than the CO (1-0) nuclear disk and core reported by Koda et al. (2002).

Direct comparisons of our results with those at other wavelengths may help clarify the origin of this excess line broadening. In the top row of Figure 12, the contours of the [C II] 158 Δv_{50} and $\Delta W_{1\sigma}$ residuals are overlaid on the 1.4 GHz image from Sebastian et al. (2019), where the double-lobed radio morphology of the wind is outlined by bright filaments. At the base of the W lobe, where the radio filaments are brightest, Δv_{50} appears to trace the lobe's edges. The material along the southern edge is receding with $\Delta v_{50} \sim +35$ km s^{-1} while it is approaching along the northern edge with $\Delta v_{50} \sim -15$ km s^{-1}.

The middle row of Figure 12 shows the same contours as above, but overlaid on the continuum subtracted Hα + [N II] image from Cecil et al. (2001), where only the eastern bubble is visible out to ~ 1 kpc above the disk (the western bubble lies behind the disk of galaxy and is therefore extinguished although not completely absent; Veilleux et al. 1994). While there is a lack of radio emission along the southern edge of the eastern bubble, the strong optical line emission in this region coincides with approaching [C II] 158 line emitting material with $\Delta v_{50} \sim -35$ km s^{-1} and where $\Delta W_{1\sigma}$ are the largest (~ 100 km s^{-1}). Cecil et al. (2001) have shown that the base of this filament aligns with the axis of the jet observed at 8 GHz (Trotter et al. 1998). The larger dispersion residuals observed here mimic those seen in the optical lines (Veilleux et al. 1994; Cecil et al. 2001) and likely have the same origin: the jet is interacting with the ISM of the galaxy disk, depositing its kinetic energy to drive the bubble (Middelberg et al. 2007). Note however that $W_{1\sigma}$ of Hα reaches up to ~ 1000 km s^{-1}, considerably larger than the [C II] widths. The [C II] 158 widths are similar to the values derived by Hawarden et al. (1995) from H$_2$ ro-vibrational transitions and mapped by Israel et al. (1998).

Beyond ~ 1 kpc, the southern optical line filament in the eastern bubble appears to break out into smaller clouds at the location where the radio emission begins. The values of [C II] Δv_{50} along this filament are ~ -20 km s^{-1}. In contrast, the base of the northern filament in the eastern bubble is seen in both optical and radio, and the [C II]-emitting is receding at velocities $\Delta v_{50} \sim 45$ km s^{-1}.

The bottom row of Figure 12 shows the [C II] 158 Δv_{50} and $\Delta W_{1\sigma}$ contours overlaid on the *HST* image from above (red and green) and the *Chandra* data from Cecil et al. (2002). Notice that on the East side, the (soft) X-ray filaments spatially correlate with the optical filaments, while in the West, the (soft) X-ray emission
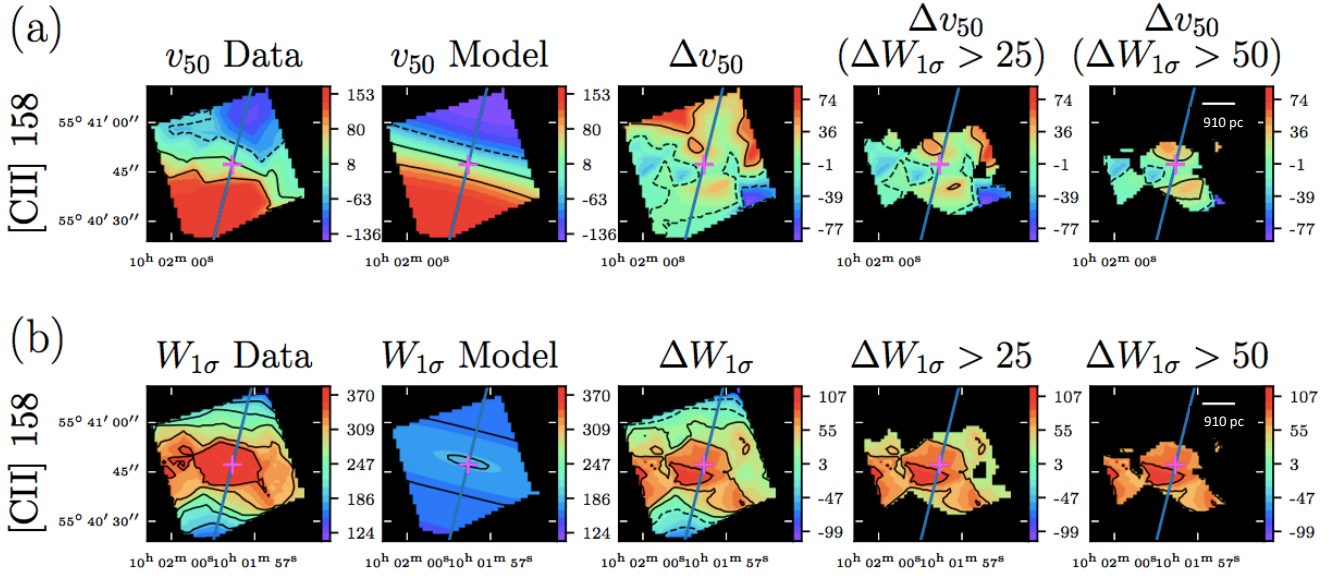
Figure 11. Results from modeling the [C II] 158 disk velocity field (a) and line widths (b) of NGC 3079 with ^{3D}ʙᴀʀᴏʟᴏ (which accounts for both the instrumental spectral and spatial resolutions), and the location of the outflow based on excess line broadening. The values of the color bar are in units of $km\,s^{-1}$. For each row of panels, we show from left to right the observed data, the best-fit model, the data − model residuals, the spatial location of the wind in regions where $\Delta W_{1\sigma} > 25\ km\,s^{-1}$, and the spatial location of the wind in regions where $\Delta W_{1\sigma} > 50\ km\,s^{-1}$. Contours in (a) are in five equal steps between the minimum and maximum velocities in each image. Contours in (b) are 0.3, 0.5, 0.7, and 0.9 of the peak value in each image. The solid blue line marks the galaxy major axis. The magenta cross marks the adopted galaxy center. North is up and East to the left.

fills the radio lobe region, but lacks any of the filamentary structures seen at 1.4 GHz. The $\Delta W_{1\sigma}$ contours are bisymmetric like the X-ray and radio structures, providing additional support for an association with the nuclear outflow.

4.2.5 *Overall Influence of the Nuclear Outflow*

The spatial coincidence noted in Sec. 4.2.4 between the regions with anomalously high [C II] 158 line widths ($\Delta W_{1\sigma}$) and the well-known visible, radio, and X-ray features associated with the nuclear outflow in this galaxy points to a physical connection between the cool gas phase traced by [C II] 158 and the warm/hot ionized and relativisitc plasma components taking part in the outflow. The broad line profiles of OH 119 and the lack of obvious OH velocity gradient reported in Sec. 3.2.2 suggest that the influence of the nuclear outflow also extends to the molecular gas phase. However, as discussed in Section 3.2.2 (Fig. 6), OH 119 is detected in absorption in only 12-14 spaxels (each $9''.4 \times 9''.4$), or only about 9-10 spatial resolution elements (10'' FWHM), centered on the inner $\sim 30'' \times 30''$ or $\sim 3 \times 3$ kpc. The far-infrared continuum quickly drops beyond this region, making the detection of OH absorption against this continuum emission more difficult and revealing possible OH emission. These limitations prevent us from making a strong statement on the origin of the anomalous OH kinematics. While we favor an outflow origin for the broad OH profiles given the similarities with the [C II] 158 profiles, we cannot formally rule out the possibility that some of the OH line broadening is due to bar streaming or associated with fast rotational velocities in a massive core, as traced by CO (1-0) (Koda et al. 2002).

Overall, our analysis of the PACS data indicates that the cool gas traced by [C II] 158 in the nuclear region of this galaxy is influenced by the ionized + relativistic outflow. This component of the ISM has been found in some gas-rich systems to dominate the

mass budget of galactic outflows and sometimes even their energetics (e.g., Veilleux et al. 2020, and references therein). This does not seem to be the case in NGC 3079 although the limited spatial and spectral resolutions of the PACS data prevent us from carrying out a detailed dynamical analysis of the [C II] outflow. In particular, the data cannot be used to reliably decompose the [C II] flux into an outflow component and a disk component. The velocities of the cool gas traced by [C II] 158 are modest compared with the escape velocity. In most circumstances (e.g., Veilleux et al. 2020), the escape velocity in a disk galaxy can be approximated as $v_{esc} \simeq (2-3)v_{rot}$, where v_{rot} is maximum rotation speed. Kinematic modeling of the large-scale Hα velocity field in NGC 3079 (Veilleux et al. 1999) gives $v_{rot} = 250\ km\,s^{-1}$, so $v_{esc} = 500 - 750\ km\,s^{-1}$. The bulk of the outflowing cool gas will thus take part in a galactic fountain that reaches the inner CGM rather than be part of a genuine wind that escapes the host galaxy altogether. This is also likely to be the case for the neutral-gas phase traced by the blueshifted H I 21 cm absorption (Shafi et al. 2015).

While direct mechanical feedback by the cool outflow on the ISM may be limited to the inner portion of the galaxy CGM, the elevated 100-to-160 μm flux ratios of Figure 4, coincident with the brightest X-ray emission, suggest that the influence of radiative feedback may extend much further. The elevated PAH 7.7/11.3 μm ratios found by Yamagishi et al. (2010) add support to this idea. The outflowing cool gas may undergo a phase transition, becoming ionized as it travels to the halo, and may contribute to the warm and hot ionized outflows that are detected on larger scales.

5 CONCLUSIONS

We have presented the results from a photometric analysis of deep *Herschel* PACS and SPIRE far-infrared images of the nearby edge-
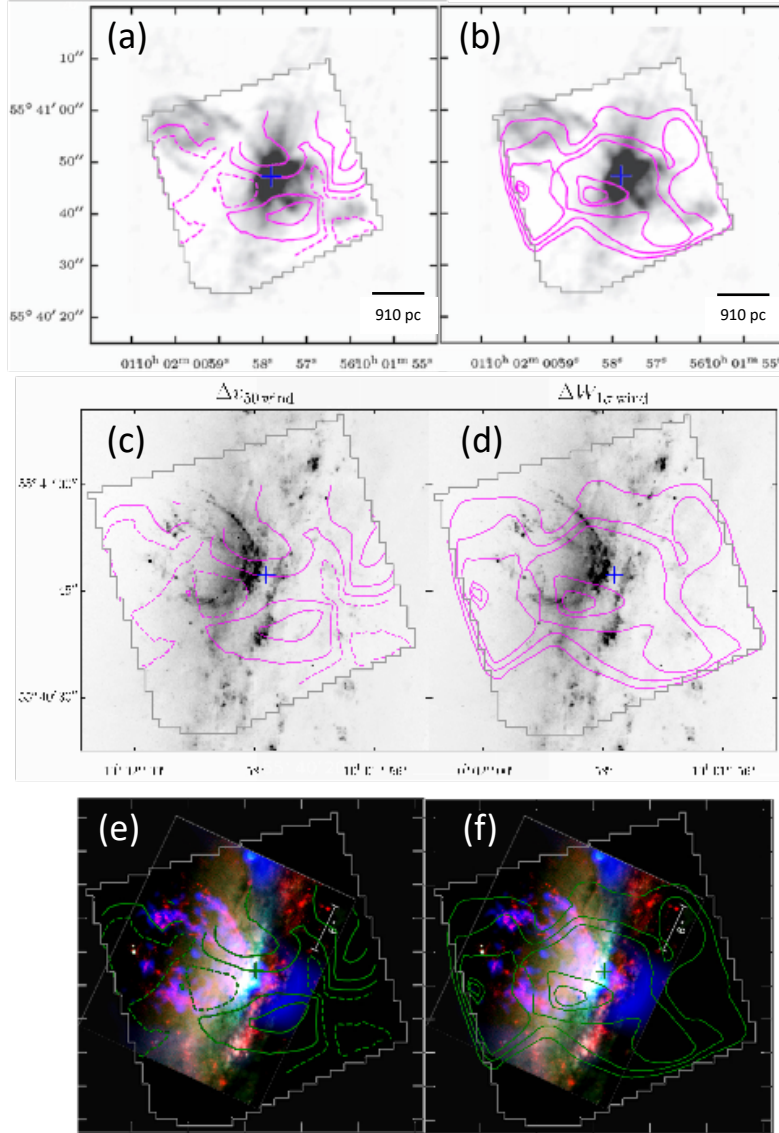
Figure 12. PACS contours of the [C II] 158 (a) v_{50} and (b) $W_{1\sigma}$ residuals in the wind in NGC 3079, overlaid on the 1.4 GHz observations from Sebastian et al. (2019). PACS contours of the [C II] 158 (c) v_{50} and (d) $W_{1\sigma}$ residuals in the wind in NGC 3079 overlaid on the Hα + [N II] image from Cecil et al. (2001). PACS contours of the [C II] 158 (e) v_{50} and (f) $W_{1\sigma}$ residuals in the wind in NGC 3079 overlaid on the *HST* image from above (red and green) and the *Chandra* data (blue) from Cecil et al. (2002). North is up and East to the left.

on disk galaxy NGC 3079, host to a well-known AGN-driven outflow. We also carried out a kinematic analysis of the [C II] 158 line emission and OH 119 line absorption within the central ~ 6 kpc region of this galaxy derived from PACS data cubes. The main results from these analyses are the following:

• The PACS images at 100 μm (PSF FWHM $\simeq 6''.8$) and 160 μm (PSF FWHM $\simeq 11''.4$) reveal a distinct X-shape structure that extends over 25×25 kpc^2 centered on the nucleus. The filaments connect back to the disk of NGC 3079, about 5 kpc on each side of the nucleus. One of the filaments is detected out to ~ 25 kpc from the nucleus and ~ 15 kpc from the galaxy disk mid-plane.

• Dust temperatures of 16-18 K and a total dust mass of $(4 - 16) \times 10^6$ $M_\odot$ are derived from fits to the far-infrared spectral energy distributions from the individual filaments making up the X-shape structure. A gas mass of $(8 - 30) \times 10^8$ $M_\odot$ is implied if the global

gas-to-dust ratio of 200 measured from the total gas and dust masses in this galaxy also applies to the X-shape structure.

• Comparisons with published data at other wavelengths suggest that the far-infrared X-shape structure is physically associated with the large-scale galactic wind detected in Hα, X-rays, and far-ultraviolet. In this picture, dusty material originally in the galactic disk of NGC 3079 is lifted above the disk and entrained in the galactic wind. The energy needed to lift this material, $\sim 10^{56}$ ergs, may have been supplied by the central AGN provided that it has maintained the same level of activity for the past $\sim 10^7$ yrs. A large mass-loading factor ($\gtrsim 100$) is implied in this scenario.

• Additional support for this scenario is found in the central 10×10 kpc region. Elevated 100-to-160 μm flux ratios, indicative of higher dust temperatures, are observed within a biconical region centered on the nucleus, coincident with the brightest soft X-ray emission. A similar coincidence between warm dust and X-

ray emission has been reported by our group in NGC 4631 (Paper I) and NGC 891 (Paper III). In NGC 3079, dust inside the bicone may be heated by UV radiation from the AGN, X-ray emission from the hot plasma in the halo, or shocks associated with the large-scale outflow into the halo.

- To survive, the dust must be shielded from fast shocks. A thermal sputtering timescale of $\sim 10^7$ yrs is derived if the hot X-ray emitting material in the X-shape filaments is in contact with the dust. This timescale is similar to the duration of the AGN jet cycle needed to produce the far-infrared X-shape structure.

- A careful analysis with ^{3D}BAROLO of the [C II] kinematics in the inner 6×6 kpc^2 derived from the PACS data cube reveals line broadening along the minor axis of this galaxy that is well in excess of the values expected from beam smearing of the disk rotational motion. The region of excess line broadening coincides loosely with the bisymmetric superbubbles and filaments seen in Hα, soft X-rays, and at radio wavelengths. This is interpreted as a sign that the nuclear warm/hot ionized + relativistic outflows in this object is stirring the cool gas traced by [C II]. The disturbed OH kinematics in this same region suggest that the molecular gas is also influenced by the nuclear outflow, although the presence of a bar and compact nuclear core makes this conclusion less certain than in the case of the cool gas.

The *Herschel* far-infrared data trace the complex interplay of the cool gas/dust with the warm/hot ionized + relativistic phases of the large-scale outflow detected at other wavelengths. The cool gas entrained in the inner hot/relativistic outflow has modest velocities relative to the escape velocity of the host, so it will eventually be deposited in the halo of the galaxy and contribute to building up the gas, dust, and metal contents of the inner CGM. The exact fate of this material is not constrained by our data. It may experience a phase transition from neutral to ionized due to AGN photoionization and/or shocks as it propagates outward into the halo. However, without a sustained source of energy from the AGN or nuclear starburst, the material in the bicone will cool down and rain back onto the galaxy disk, closing the loop of a large-scale galactic fountain. Deeper and higher resolution infrared data of this and other nearby galaxies with the upcoming *James Webb Space Telescope* and planned *Origins Space Telescope* will provide unique insights into this disk-halo gas circulation pattern which is believed to regulate the evolution of disk galaxies such as our own.

DATA AVAILABILITY

The data underlying this article will be shared on reasonable request to the corresponding author.

REFERENCES

Aniano G., Draine B. T., Gordon K. D., Sandstrom K., 2011, PASP, 123, 1218
Arendt R. G., et al., 2010, ApJ, 725, 585
Biscaro C., Cherchneff I., 2014, A&A, 564, A25
Biscaro C., Cherchneff I., 2016, A&A, 589, A132
Bland-Hawthorn J., Gerhard O., 2016, ARA&A, 54, 529
Bosma A., 1978, PhD thesis, -
Brightman M., et al., 2015, ApJ, 805, 41
Burchett J. N., Rubin K. H. R., Prochaska J. X., Coil A. L., Vaught R. R., Hennawi J. F., 2021, ApJ, 909, 151
Carilli C. L., Walter F., 2013, ARA&A, 51, 105
Cecil G., Bland-Hawthorn J., Veilleux S., Filippenko A. V., 2001, ApJ, 555, 338
Cecil G., Bland-Hawthorn J., Veilleux S., 2002, ApJ, 576, 745
Chevalier R. A., Clegg A. W., 1985, Nature, 317, 44
Contursi A., et al., 2013, A&A, 549, A118
Cooper J. L., Bicknell G. V., Sutherland R. S., Bland-Hawthorn J., 2008, ApJ, 674, 157
Devereux N. A., Young J. S., 1990, ApJ, 359, 42
Di Teodoro E. M., Fraternali F., 2015, MNRAS, 451, 3021
Dopita M. A., Seitenzahl I. R., Sutherland R. S., Vogt F. P. A., Winkler P. F., Blair W. P., 2016, ApJ, 826, 150
Draine B. T., 2003, ARA&A, 41, 241
Draine B. T., et al., 2007, ApJ, 663, 866
Duric N., Seaquist E. R., Crane P. C., Bignell R. C., Davis L. E., 1983, ApJ, 273, L11
Fabbiano G., Kim D. W., Trinchieri G., 1992, ApJS, 80, 531
Filippenko A. V., Sargent W. L. W., 1992, AJ, 103, 28
Ford H. C., Dahari O., Jacoby G. H., Crane P. C., Ciardullo R., 1986, ApJ, 311, L7
Gall C., Hjorth J., 2018, ApJ, 868, 62
Gall C., et al., 2014, Nature, 511, 326
Galliano F., Galametz M., Jones A. P., 2018, ARA&A, 56, 673
Griffin M. J., et al., 2010, A&A, 518, L3
Hawarden T. G., Israel F. P., Geballe T. R., Wade R., 1995, MNRAS, 276, 1197
Heckman T. M., Armus L., Miley G. K., 1990, ApJS, 74, 833
Hodges-Kluck E. J., Yukita M., Tanner R., Ptak A. F., Bregman J. N., Li J.-t., 2020, ApJ, 903, 35
Högbom J. A., 1974, A&AS, 15, 417
Hollenbach D. J., Tielens A. G. G. M., 1997, ARA&A, 35, 179
Hopkins P. F., Quataert E., Murray N., 2012, MNRAS, 421, 3522
Howk J. C., Savage B. D., 1997, AJ, 114, 2463

Hu C.-Y., Zhukovska S., Somerville R. S., Naab T., 2019, MNRAS, 487, 3252

Humphreys R. M., Davidson K., Jones T. J., Pogge R. W., Grammer S. H., Prieto J. L., Pritchard T. A., 2012, ApJ, 760, 93

Irwin J. A., Saikia D. J., 2003, MNRAS, 346, 977

Irwin J. A., Seaquist E. R., 1988, ApJ, 335, 658

Irwin J. A., Seaquist E. R., 1991, ApJ, 371, 111

Irwin J. A., Seaquist E. R., Taylor A. R., Duric N., 1987, ApJ, 313, L91

Irwin J., et al., 2019, AJ, 158, 21

Israel F. P., van der Werf P. P., Hawarden T. G., Aspin C., 1998, A&A, 336, 433

Iyomoto N., Fukazawa Y., Nakai N., Ishihara Y., 2001, ApJ, 561, L69

Kochanek C. S., 2011, ApJ, 743, 73

Koda J., Sofue Y., Kohno K., Nakanishi H., Onodera S., Okumura S. K., Irwin J. A., 2002, ApJ, 573, 105

Kondratko P. T., Greenhill L. J., Moran J. M., 2005, ApJ, 618, 618

Lakićević M., et al., 2015, ApJ, 799, 50

Li J.-T., Hodges-Kluck E., Stein Y., Bregman J. N., Irwin J. A., Dettmar R.-J., 2019, ApJ, 873, 27

Lochhaas C., Thompson T. A., Quataert E., Weinberg D. H., 2018, MNRAS, 481, 1873

Masini A., et al., 2016, A&A, 589, A59

Matsuura M., et al., 2019, MNRAS, 482, 1715

McCormick A., Veilleux S., Rupke D. S. N., 2013, ApJ, 774, 126

McCormick A., et al., 2018, MNRAS, 477, 699

Meléndez M., Mushotzky R. F., Shimizu T. T., Barger A. J., Cowie L. L., 2014, ApJ, 794, 152

Meléndez M., et al., 2015, ApJ, 804, 46

Ménard B., Scranton R., Fukugita M., Richards G., 2010, MNRAS, 405, 1025

Middelberg E., Agudo I., Roy A. L., Krichbaum T. P., 2007, MNRAS, 377, 731

Nozawa T., Kozasa T., Habe A., 2006, ApJ, 648, 435

Ott S., 2010, in Mizumoto Y., Morita K. I., Ohishi M., eds, Astronomical Society of the Pacific Conference Series Vol. 434, Astronomical Data Analysis Software and Systems XIX. p. 139 (`arXiv:1011.1209`)

Peek J. E. G., Ménard B., Corrales L., 2015, ApJ, 813, 7

Péroux C., Howk J. C., 2020, ARA&A, 58, 363

Poglitsch A., et al., 2010, A&A, 518, L2

Ricci C., et al., 2017, ApJS, 233, 17

Rogstad D. H., Lockhart I. A., Wright M. C. H., 1974, ApJ, 193, 309

Roussel H., 2013, PASP, 125, 1126

Rupke D. S. N., et al., 2019, Nature, 574, 643

Seale J. P., Looney L. W., Wong T., Ott J., Klein U., Pineda J. L., 2012, ApJ, 751, 42

Sebastian B., Kharb P., O'Dea C. P., Colbert E. J. M., Baum S. A., 2019, ApJ, 883, 189

Shafi N., Oosterloo T. A., Morganti R., Colafrancesco S., Booth R., 2015, MNRAS, 454, 1404

Sharp R. G., Bland-Hawthorn J., 2010, ApJ, 711, 818

Shimizu T. T., Meléndez M., Mushotzky R. F., Koss M. J., Barger A. J., Cowie L. L., 2016, MNRAS, 456, 3335

Shopbell P. L., Bland-Hawthorn J., 1998, ApJ, 493, 129

Silvia D. W., Smith B. D., Shull J. M., 2010, ApJ, 715, 1575

Sofue Y., Irwin J. A., 1992, PASJ, 44, 353

Sofue Y., Koda J., Kohno K., Okumura S. K., Honma M., Kawamura A., Irwin J. A., 2001, ApJ, 547, L115

Springob C. M., Masters K. L., Haynes M. P., Giovanelli R., Marinoni C., 2007, ApJS, 172, 599

Sternberg A., Dalgarno A., 1995, ApJS, 99, 565

Stone M., 2020, PhD thesis, University of Maryland, College Park

Stone M., Veilleux S., Meléndez M., Sturm E., Graciá-Carpio J., González-Alfonso E., 2016, ApJ, 826, 111

Strickland D. K., Heckman T. M., Colbert E. J. M., Hoopes C. G., Weaver K. A., 2004a, ApJS, 151, 193

Strickland D. K., Heckman T. M., Colbert E. J. M., Hoopes C. G., Weaver K. A., 2004b, ApJ, 606, 829

Temim T., Dwek E., Tchernyshyov K., Boyer M. L., Meixner M., Gall C., Roman-Duval J., 2015, ApJ, 799, 158

Tielens A. G. G. M., Hollenbach D., 1985, ApJ, 291, 722

Trotter A. S., Greenhill L. J., Moran J. M., Reid M. J., Irwin J. A., Lo K.-Y., 1998, ApJ, 495, 740

Tumlinson J., Peeples M. S., Werk J. K., 2017, ARA&A, 55, 389

Veilleux S., Cecil G., Bland-Hawthorn J., Tully R. B., Filippenko A. V., Sargent W. L. W., 1994, ApJ, 433, 48

Veilleux S., Cecil G., Bland-Hawthorn J., 1995, ApJ, 445, 152

Veilleux S., Bland-Hawthorn J., Cecil G., 1999, AJ, 118, 2108

Veilleux S., Cecil G., Bland-Hawthorn J., 2005, ARA&A, 43, 769

Veilleux S., et al., 2013, ApJ, 776, 27

Veilleux S., Maiolino R., Bolatto A. D., Aalto S., 2020, A&ARv, 28, 2

Wilson A. S., Tsvetanov Z. I., 1994, AJ, 107, 1227

Yamagishi M., Kaneda H., Ishihara D., Komugi S., Suzuki T., Onaka T., 2010, PASJ, 62, 1085

Yamauchi A., Nakai N., Sato N., Diamond P., 2004, PASJ, 56, 605

Yoon J. H., et al., 2021, MNRAS, 502, 969

Young J. S., Claussen M. J., Scoville N. Z., 1988, ApJ, 324, 115

This paper has been typeset from a TEX/LATEX file prepared by the author.